



# **Three-Dimensional Geologic Map of the Southeastern Gabbs Valley Geothermal Area, Nevada**

By Drew L. Siler, Jeffrey B. Witter, Jason W. Craig, Tait E. Earney, William D. Schermerhorn,  
Dominique Fournier, James E. Faulds, Jonathan M.G. Glen, and Jared R. Peacock

Pamphlet to accompany

**Scientific Investigations Map 3498**

2023

**U.S. Department of the Interior  
U.S. Geological Survey**

## U.S. Geological Survey, Reston, Virginia: 2023

For more information on the USGS—the Federal source for science about the Earth, its natural and living resources, natural hazards, and the environment—visit <https://www.usgs.gov> or call 1–888–ASK–USGS.

For an overview of USGS information products, including maps, imagery, and publications, visit <https://store.usgs.gov>.

Any use of trade, firm, or product names is for descriptive purposes only and does not imply endorsement by the U.S. Government.

Although this information product, for the most part, is in the public domain, it also may contain copyrighted materials as noted in the text. Permission to reproduce copyrighted items must be secured from the copyright owner.

### Suggested citation:

Siler, D.L., Witter, J.B., Craig, J.W., Earney, T.E., Schermerhorn, W.D., Fournier, D., Faulds, J.E., Glen, J.M.G., and Peacock, J.R., 2023, Three-dimensional geologic map the southeastern Gabbs Valley geothermal area, Nevada: U.S. Geological Survey Scientific Investigations Map 3498, 23 p., 1 sheet, <https://doi.org/10.3133/sim3498>.

### Associated data for this publication:

Siler, D.L., 2022, Stratigraphic and fault surfaces from the three-dimensional geologic map of the southeastern Gabbs Valley geothermal area: U.S. Geological Survey data release, <https://doi.org/10.5066/P9BR3681>.

# Contents

- Abstract ..... 1
- Purpose and Scope ..... 1
- Introduction..... 1
- Geologic Setting..... 3
- Data ..... 3
  - Gravity Data ..... 3
  - Magnetic Data..... 6
  - Geologic Cross Sections and 2D Potential-Field Forward Models ..... 6
- 3D Geologic Mapping Methods..... 9
  - 3D Fault Mapping ..... 9
  - 3D Stratigraphic Mapping ..... 9
- 3D Gravity Inversion Modeling ..... 9
  - Inversion Modeling Methods..... 10
  - Adjustment of the 3D Map Based on Inversion Results..... 10
    - Round 1—The Initial 3D Geologic Map and Density Model..... 12
    - Round 2—Version 2 Geologic Map and Density Model..... 13
    - Round 3—Version 3 Geologic Map and Density Model..... 13
    - Round 4—Version 4 Geologic Map and Density Model..... 14
- Comparison of the Density Inversion Models..... 17
- Structure of the 3D Geologic Map ..... 18
- Stratigraphy of the 3D Geologic Map ..... 18
  - The Southeastern Gabbs Valley Geothermal System..... 18
- Potential Applications for the 3D Geologic Map ..... 18
  - Conventional Geothermal Research and Resource Assessment..... 18
  - Reservoir Modeling and Management ..... 19
  - Seismic Hazard Analysis ..... 19
  - Basin Hydrogeology ..... 19
  - Education and Scientific Inquiry ..... 19
- Acknowledgments ..... 19
- Description of Map Units..... 19
  - Sedimentary Deposits ..... 19
  - Bedrock ..... 20
    - Volcanic Rocks..... 20
    - Crystalline Basement Rocks ..... 20
- References Cited..... 20

## Figures

1. Generalized geologic map of the region surrounding the southeastern Gabbs Valley study area .....	2
2. Geologic map of southeastern Gabbs Valley geothermal area .....	4
3. Map of complete Bouguer gravity anomaly (CBA), the locations of gravity stations, and the maximum horizontal gradients in the CBA.....	5
4. Map of reduced-to-pole magnetic field, magnetic data, and the locations of the maximum horizontal gradients in reduced-to-pole magnetics.....	7
5. Potential-field forward models and geologic cross section for $A-A'$ .....	8
6. Maps of misfit between the observed complete Bouguer gravity anomaly (CBA) and calculated gravity for the four gravity inversions at the 472 gravity stations within the inversion model area.....	11
7. Three-dimensional density models for each round of gravity inversion modeling, sliced along cross section $B-B'$ .....	12
8. Three-dimensional (3D) density models for each round of gravity inversion modeling, showing the model volumes that have density greater than 2,550 kilograms per cubic meter .....	13
9. Histograms of density distributions in each stratigraphic unit for each round of gravity inversion modeling .....	14
10. Maps of 'difference surfaces,' the difference in elevation for the top surface of the four stratigraphic units altered during adjustments to the map based on 3D gravity inversion modeling .....	16

## Tables

1. Magnetic and density properties used in gravity and magnetic forward modeling and as initial densities in three-dimensional gravity inversion modeling .....	6
2. Calculated density model results for four three-dimensional gravity inversions (versions 1–4) .....	15

## Conversion Factors

U.S. customary units to International System of Units

Multiply	By	To obtain
Length		
inch (in.)	25.4	millimeter (mm)
foot (ft)	0.3048	meter (m)
mile (mi)	1.609	kilometer (km)
Area		
square mile (mi <sup>2</sup> )	2.590	square kilometer (km <sup>2</sup> )
Volume		
cubic foot (ft <sup>3</sup> )	0.02832	cubic meter (m <sup>3</sup> )
Flow rate		
inch per year (in/yr)	25.4	millimeter per year (mm/yr)
Mass		
pound, avoirdupois (lb)	0.4536	kilogram (kg)
Density		
pound per cubic foot (lb/ft <sup>3</sup> )	16.02	kilogram per cubic meter (kg/m <sup>3</sup> )

Temperature in degrees Celsius (°C) may be converted to degrees Fahrenheit (°F) as  
 $^{\circ}\text{F} = (1.8 \times ^{\circ}\text{C}) + 32$ .

Temperature in degrees Fahrenheit (°F) may be converted to degrees Celsius (°C) as  
 $^{\circ}\text{C} = (^{\circ}\text{F} - 32) / 1.8$ .

## Abbreviations

CBA complete Bouguer anomaly

ka kilo-annum

*M* Magnitude

mGal milliGal

MWe megawatt electrical

2D two-dimensional

3D three-dimensional



# Three-Dimensional Geologic Map of the Southeastern Gabbs Valley Geothermal Area, Nevada

By Drew L. Siler,<sup>1,2</sup> Jeffrey B. Witter,<sup>3</sup> Jason W. Craig,<sup>4</sup> Tait E. Earney,<sup>1</sup> William D. Schermerhorn,<sup>1</sup> Dominique Fournier,<sup>5</sup> James E. Faulds,<sup>4</sup> Jonathan M.G. Glen,<sup>1</sup> and Jared R. Peacock<sup>1</sup>

## Abstract

This three-dimensional (3D) geologic map displays the subsurface geology in the upper ~4 kilometers of the Earth's crust in the southeastern Gabbs Valley geothermal area of west-central Nevada. The 3D map was constructed by integrating the results from detailed geologic mapping, 3D gravity inversion modeling, and potential-field-geophysical studies. This effort was undertaken as part of the Nevada Play Fairway Project, a regional effort to characterize new geothermal resources in the United States. Local data collection and analysis in southeastern Gabbs Valley, Nevada, including the construction of this 3D map, led to the drilling of six temperature gradient wells and identification of previously unknown hydrothermal fluids at 150 meters depth. The measured temperatures, which are as high as 124.9 degrees Celsius, indicate that the southeastern Gabbs Valley hydrothermal system has temperatures that are comparable to geothermal fields that have been developed for electricity generation in the region. We describe the geologic units and structures displayed by the map and discuss the methods used to integrate the geologic and geophysical information into the 3D geologic interpretation. The accompanying map provides horizontal and vertical section views and oblique perspective views from several angles. The digital data for elements of the map, the individual 3D fault surfaces, and stratigraphic surfaces are available from Siler (2022). The accompanying map sheet and video displaying the 3D map are available at <https://doi.org/10.3133/sim3498>.

## Purpose and Scope

This three-dimensional (3D) geologic map was constructed to describe the local fault structure and stratigraphy within southeastern Gabbs Valley and assess previously unknown

geothermal resources in the study area. The study area is in southeastern Gabbs Valley, a ~700 square kilometer (km<sup>2</sup>) valley located in west-central Nevada. The study area is approximately 20 kilometers (km) southwest of the town of Gabbs, Nevada, and 50 km east-northeast of the town of Hawthorne, Nevada (fig. 1). The town of Gabbs is located on the eastern side of Gabbs Valley, which is otherwise sparsely inhabited and largely undeveloped.

Electricity can be produced using the heat extracted from hydrothermal fluids occurring naturally in the subsurface. This is referred to as geothermal energy. More than 670 megawatt electrical (MWe) geothermal electricity generation capacity currently exists in the Great Basin, and regional analysis indicates that far greater power production is possible (Williams and others, 2007, 2008, 2009; Hamm and others, 2019). In this region, geothermal energy is produced from fluids that range from 97 to 187 degrees Celsius (°C; Ayling, 2020). Geothermal fields typically occur in areas where faults intersect or interact with one another in specific geometries (Faulds and others, 2006, 2011, 2015). This 3D map characterizes the subsurface fault structure in southeastern Gabbs Valley to assess previously unknown geothermal resources in the area. This publication consists of this pamphlet, one map sheet showing oblique, plan, and cross-sectional views through the 3D map, and one video showing the 3D map from multiple angles. The digital data for the individual 3D fault and stratigraphic surfaces are available from Siler (2022).

## Introduction

Because of its location at a displacement transfer zone between young strike-slip and normal fault systems and relatively high geothermometric temperatures, the southeastern Gabbs Valley area emerged from the Nevada Play Fairway Project as a favorable site for assessment of previously undiscovered geothermal resources (Faulds and others, 2015a, b, 2016a, b). The Nevada Play Fairway Project effort focused on integration of regional-scale parameters indicative of geothermal activity, including geological, geophysical, and geochemical data to identify local areas of interest for new geothermal resources in

<sup>1</sup>U.S. Geological Survey.

<sup>2</sup>Now at Geologica Geothermal Group, Inc.

<sup>3</sup>Innovate Geothermal Ltd.

<sup>4</sup>Nevada Bureau of Mines and Geology.

<sup>5</sup>University of British Columbia.

the United States. After areas of interest, including southeastern Gabbs Valley, were identified, local studies aimed at identification and characterization of new geothermal resources were conducted (Faulds and others, 2015a, b, 2016a, b; McClain and others, 2015; Shervais and others, 2015, 2017; Ito and others, 2017; Lautze and others, 2017; Siler and others, 2017).

Prior to this study and associated work (Craig and others, 2017; Craig, 2018; Faulds and others, 2018; Peacock and others,

2018; Earney and others, 2019; Craig and others, 2021), there were no known geothermal resources in the southeastern part of Gabbs Valley. However, two known hydrothermal systems occur in the western part of Gabbs Valley. The Don A. Campbell geothermal system lies ~16.5 km northwest of the study area, and supports a 39 MWe power station generating electricity from ~125 °C hydrothermal fluids (Orenstein and Delwiche, 2014), and Rawhide Hot Springs, ~12 km north of the study area (fig. 1), which has a

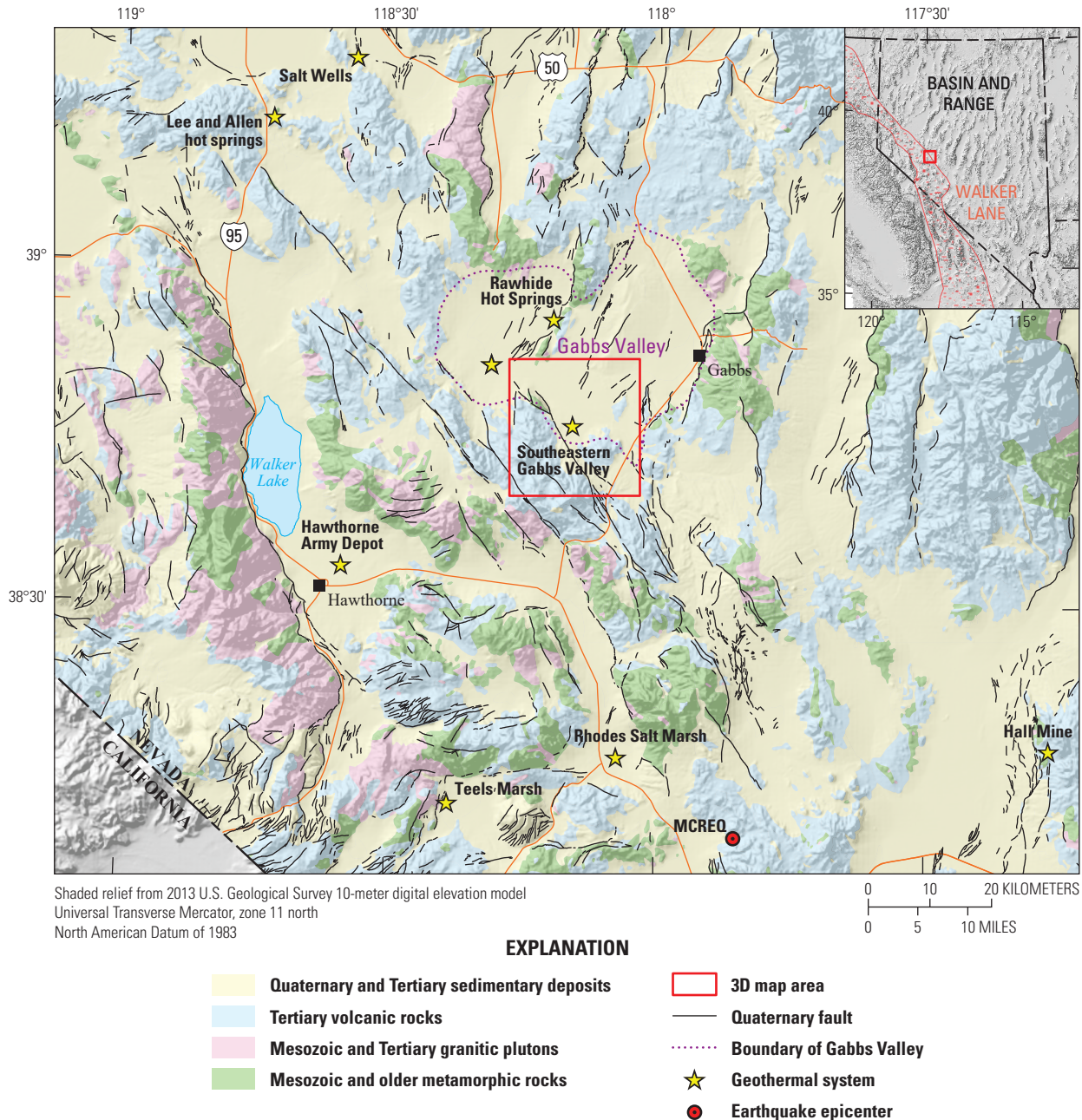


**Figure 1.** Generalized geologic map of the region surrounding the southeastern Gabbs Valley study area (modified from Crafford, 2010). Red boxes on main figure and inset regional map show the location of the study area and figures 2–4. The Basin and Range and Walker Lane tectonic provinces are shown in the inset. The hydrothermal systems shown have a measured or estimated temperature greater than 120 degrees Celsius (yellow star); data from Faulds and others (2006, 2011, 2021). MCREQ shows the epicenter (red circle) of the 2020 magnitude 6.5 Monte Cristo Range earthquake (data from the U.S. Geological Survey Earthquake Hazards Program and Nevada Seismological Laboratory, <https://earthquake.usgs.gov/earthquakes/eventpage/nn00725272/executive>). Quaternary faults from Crafford (2007) and U.S. Geological Survey Quaternary fault and fold database (U.S. Geological Survey, 2006). 3D, three-dimensional.

surface temperature of ~60 °C and geochemical indications of temperatures as high as ~130–140 °C (Kratt and others, 2008).

This 3D geologic map builds upon the regional Nevada Play Fairway Project (Faulds and others, 2015a, b, 2016a, b) and was constructed to characterize the geologic structure of the southeastern Gabbs Valley geothermal area and help site temperature gradient wells (Craig and others, 2017; Craig, 2018; Faulds and others, 2018; Peacock and others, 2018; Earney and others, 2019; Craig and others, 2021). Six 150-meter (m)-deep temperature gradient wells were sited and drilled, two of which confirmed the presence of a formerly unknown hydrothermal system with temperatures of at least 114.5 to 124.9 °C (Craig and others, 2017; Faulds and others, 2018; Craig and others, 2021).

The 3D geologic map displays subsurface fault surfaces, stratigraphic contacts, and rock volumes that are informed by 1:24,000-scale geologic mapping (Craig and others, 2017; Craig, 2018; Craig and others, 2021), 2D geologic cross sections (Craig and others, 2017; Craig, 2018; Craig and others, 2021) that were iteratively constructed with 2D forward models of gravity and magnetic data (Earney, and others, 2018), interpretation of gravity and magnetic anomalies and horizontal gradients (Earney, and others, 2018), and iterative 3D gravity inversion modeling. In addition to conventional geothermal research and resource assessment, potential applications of this map include seismicity hazard analysis, basin hydrogeology, and education and scientific inquiry (see “Potential Applications for 3D Map” section of this report).

## Geologic Setting

Gabbs Valley, located in west-central Nevada, is a composite structural basin along the transition between the Walker Lane and the Basin and Range tectonic provinces (fig. 1; Oldow, 1992; Wernicke, 1992; Faulds and others, 2005; Colgan and others, 2006). The two major fault systems in the study area are: (1) west-northwest to northwest striking, predominantly steeply dipping, dextral strike-slip faults and (2) north-northeast to northeast striking normal faults (fig. 2). Both major fault systems are younger than 15 thousand years and reflect the differing styles of tectonism of the Walker Lane and Basin and Range Provinces, respectively. The Petrified Springs Fault, a northwest striking dextral strike-slip fault (slip rate=0.6±0.1 millimeters per year; Angster, 2018) has been active in the past 15 thousand years (Wesnousky, 2005), whereas historical ruptures associated with the 1932 Cedar Mountain earthquake constitute part of the north-northeast to northeast striking fault system (fig. 2; Bell and others, 1999). These two fault systems intersect in the center of the study area in a displacement transfer zone (Faulds and others, 2006; Faulds and Hinz, 2015a). Here, northwest directed dextral shear along the Petrified Springs Fault and other Walker Lane dextral faults is transferred to west-northwest directed extension on the north-northeast to northeast striking normal and dextral normal faults of the Basin and Range Province (fig. 2).

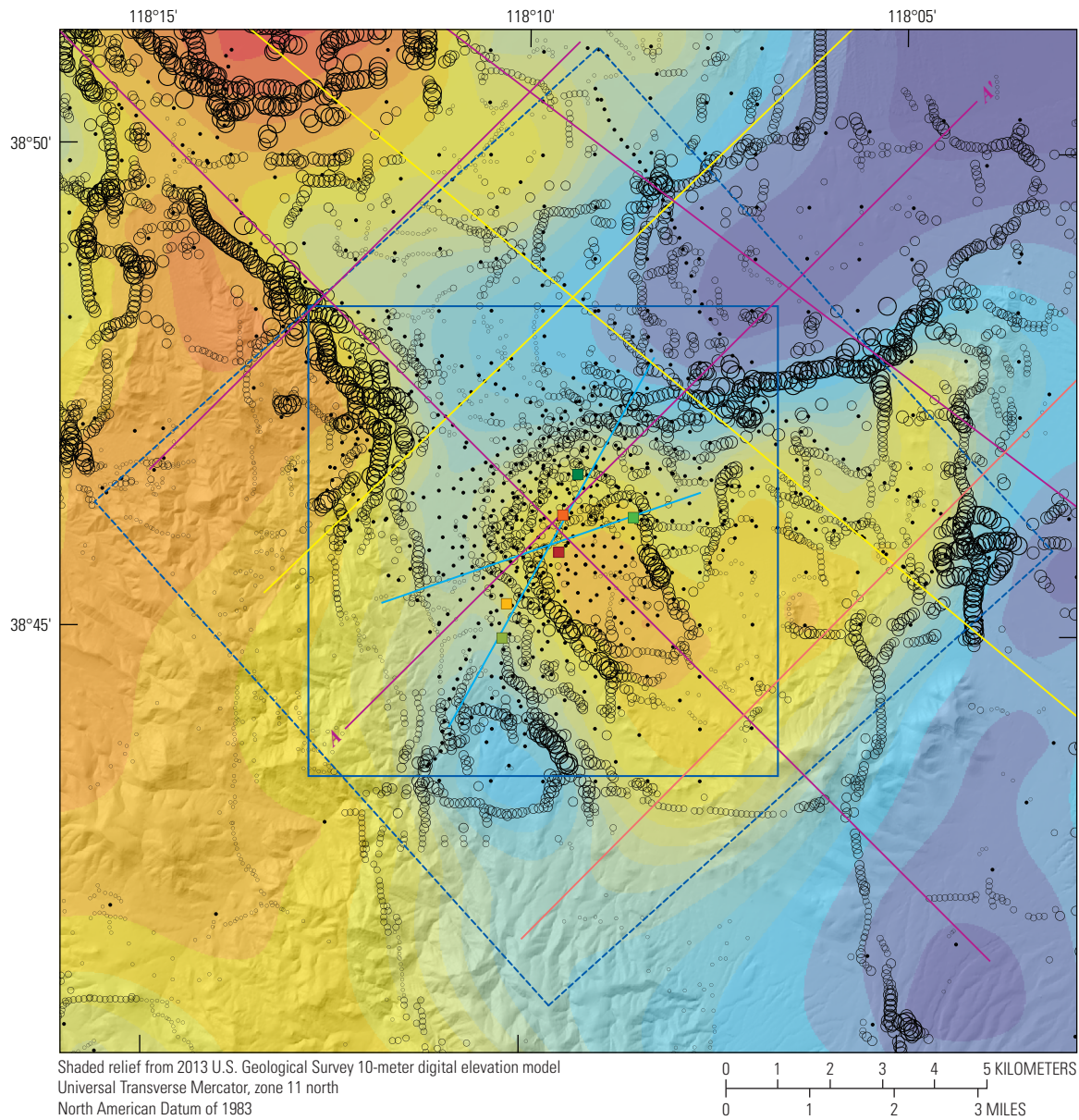
The Gabbs Valley basin is floored by Upper Triassic metasedimentary and metavolcanic basement rocks of the Luning Formation, consisting of metamorphosed turbidite sequences, including thin-bedded conglomerate, siltstone, claystone, sandstone and limestone as well as interbedded lava flows and volcaniclastic rocks. The metamorphic basement rocks are unconformably overlain by Miocene rhyodacite tuffs, largely the Poinsettia Tuff Member of the Hu-pwi Rhyodacite, as well as Miocene rhyolitic, andesitic, and basaltic lava flows and tuffs. The Miocene volcanic rocks are overlain by the Miocene Esmeralda Formation, which consists of tuffaceous siltstone, fluviolacustrine siltstone, sandstone, and mudstone. The Miocene sedimentary rocks are overlain by Pliocene to Quaternary alluvial, colluvial, eolian, and playa sediments and sedimentary rocks (figs. 1, 2; Ekren and others, 1980; Ekren and Byers, 1985, 1986a, b; Craig and others, 2017; Craig, 2018; Craig and others, 2021).

## Data

### Gravity Data

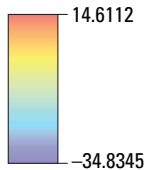
The gravity data used in the construction of the 3D geologic map consist of ~3,500 gravity stations within a 60 km radius from the center of the study area. This includes 703 stations within the boundaries of the 3D map. Typical station spacing is ~250–500 m, generally increasing to ~1,000 m near the boundaries of the inversion model area (fig. 3). Gravity data processing followed the methods of Blakely and others (1995). Multiple test inversions indicated that 2,620 kilograms per cubic meter (kg/m<sup>3</sup>) best represents the average density of the subsurface; therefore, complete Bouguer anomaly (CBA) values were calculated using this density. No regional gravity trend was removed from the data prior to geophysical modeling. Visual assessment of gravity data in the Gabbs Valley area indicates that any regional gravity signal is weak and would have limited effect on the gravity modeling results. However, a detailed assessment of the regional gravity signal and how it may affect the gravity modeling results has not yet been conducted. The locations of maximum horizontal gradients were calculated from the CBA using methods of Blakely and Simpson (1986). These maxima define the most prevalent lateral changes in the gravity field and are typically caused by fault induced juxtaposition of geologic units that have different densities. Physical property measurements (density, magnetic remanence, and magnetic susceptibility) of 41 rock samples collected from 19 locations were used to guide geophysical modeling (Craig, 2018). The density and susceptibility values are shown in table 1. Density and susceptibility values from a database of rocks analogous to those in the study area were also used (Ponce, 2021) to guide the geophysical modeling.





**EXPLANATION**

**Complete Bouguer gravity anomaly, in milligals**



**Maximum horizontal gradient of Complete Bouguer anomaly**

- Low gradient
- (small)
- (medium)
- (large) High gradient

- 3D geologic map
- - - 3D gravity inversion model
- Geologic cross section
- Potential-field forward model section
- Paired geologic and potential-field section
- 2D forward models
- Temperature gradient well—Colors indicate relative temperature; warm colors for high temperature, cool colors for low temperature
- Gravity station



**Figure 3.** Map of complete Bouguer gravity anomaly (CBA), the locations of gravity stations, and the maximum horizontal gradients in the CBA. Geologic cross sections and potential-field forward model sections used in construction of the 3D map are shown. Section A–A', shown on figure 5 is labeled. The locations of the temperature gradient wells drilled as part of this study are colored with respect to temperature, warm colors for high temperatures, cool colors for low temperatures; measured temperatures are shown on figure 2 (Faulds and others, 2018). 3D, three dimensional; 2D, two dimensional.

**Table 1.** Magnetic and density properties used in gravity and magnetic forward modeling (fig. 5) and as initial densities in three-dimensional (3D) gravity inversion modeling (figs. 7–9).

[Geologic units are described in figure 2. kg/m<sup>3</sup>, kilogram per cubic meter; —, no data; SI, magnetic susceptibility]

Geologic unit	Measured density (kg/m <sup>3</sup> )	Number of density measurements	Density used in forward modeling and 3D inversion (kg/m <sup>3</sup> )	Magnetic susceptibility (SI)
Holocene to Miocene sediments and sedimentary rocks (unit QT)	—	—	<sup>1</sup> 2,100	<sup>1</sup> 0.00
Miocene sediments and sedimentary rocks (unit Ts)	—	—	<sup>1</sup> 2,230	<sup>1</sup> 0.00
Mafic to intermediate lavas of Mount Ferguson (Tlf)	2,460±120	35	2,460	0.007–0.014
Poinsettia Tuff Member of the Hu-pwi Rhyodacite (unit Tp)	2,250±120	2	<sup>2</sup> 2,430	<sup>3</sup> 0.021
Late Triassic metasedimentary and volcaniclastic rocks (unit Tvc)	2,670±30	4	<sup>3</sup> 2,670	<sup>3</sup> 0.001

<sup>1</sup>Density and magnetic susceptibility estimated from initial two-dimensional modeling results.

<sup>2</sup>Because samples were limited, density and magnetic susceptibility were also estimated from database of >20,000 samples from the western United States (Ponce, 2021). Database density values for rhyodacite tuff and the two measured samples did not agree; therefore, higher density values from the database, those likely more representative of the densely welded Poinsettia Tuff Member (Craig, 2018), were used.

<sup>3</sup>Because samples were limited, density and magnetic susceptibility were also taken from a database of >20,000 samples from the western United States, (Ponce, 2021). Density and susceptibility values from andesitic and dacitic lavas in the database and the six measured samples were consistent; therefore, measured density and susceptibility values were used.

## Magnetic Data

Approximately 300 km of high-resolution magnetic data were collected on foot and by use of all-terrain vehicle-magnetometer systems (Athens and others, 2011). In the center of the 3D map, line spacing is ~250 m with line spacing increasing toward the margins of the study area (fig. 4). Standard processing was applied to correct for diurnal variations of the magnetic field (Telford and others, 1990), and the data were filtered to remove anomalies associated with cars, culverts, fences, power lines, and other magnetic objects at the land surface. Reduced-to-pole magnetic anomalies and the locations of maximum horizontal gradients in the reduced-to-pole magnetic field (fig. 4) were calculated (for example, Blakely, 1995) to highlight the locations of significant changes in subsurface magnetic properties, which can be caused by fault induced juxtaposition of geologic units that have different magnetic properties. Magnetic susceptibility and remanence values were measured in the field using a ZH instruments SM30 meter (table 1). Twelve or more measurements were made across a several meter wide outcrop area to estimate susceptibility values.

## Geologic Cross Sections and 2D Potential-Field Forward Models

Five detailed geologic cross sections were constructed to help characterize the subsurface in the study area. Initial versions were published by Craig and others (2017), Craig (2018), and Craig and others (2021). Additionally, eight gravity and magnetic (potential-field) forward models were constructed by Earney and others (2018). Four of these were constructed along the same geologic cross sections from Craig and others (2017), Craig (2018), and Craig and others (2021). Figures 3 and 4 show the lines for all geologic cross sections and 2D potential-field models built as part of this study; section *A–A'* is reproduced in figure 5. After their initial development, the four coincident geologic cross sections and forward models were iteratively refined to ensure consistency between interpretations of geophysical and geologic data. Initial geologic cross section construction was informed by depth-to-basement inversion modeling of gravity data (Earney and others, 2018). Depth-to-basement modeling constituted two-layer inversions along the profiles using a basement rock density of 2,670 kg/m<sup>3</sup>. Initial geologic cross section construction

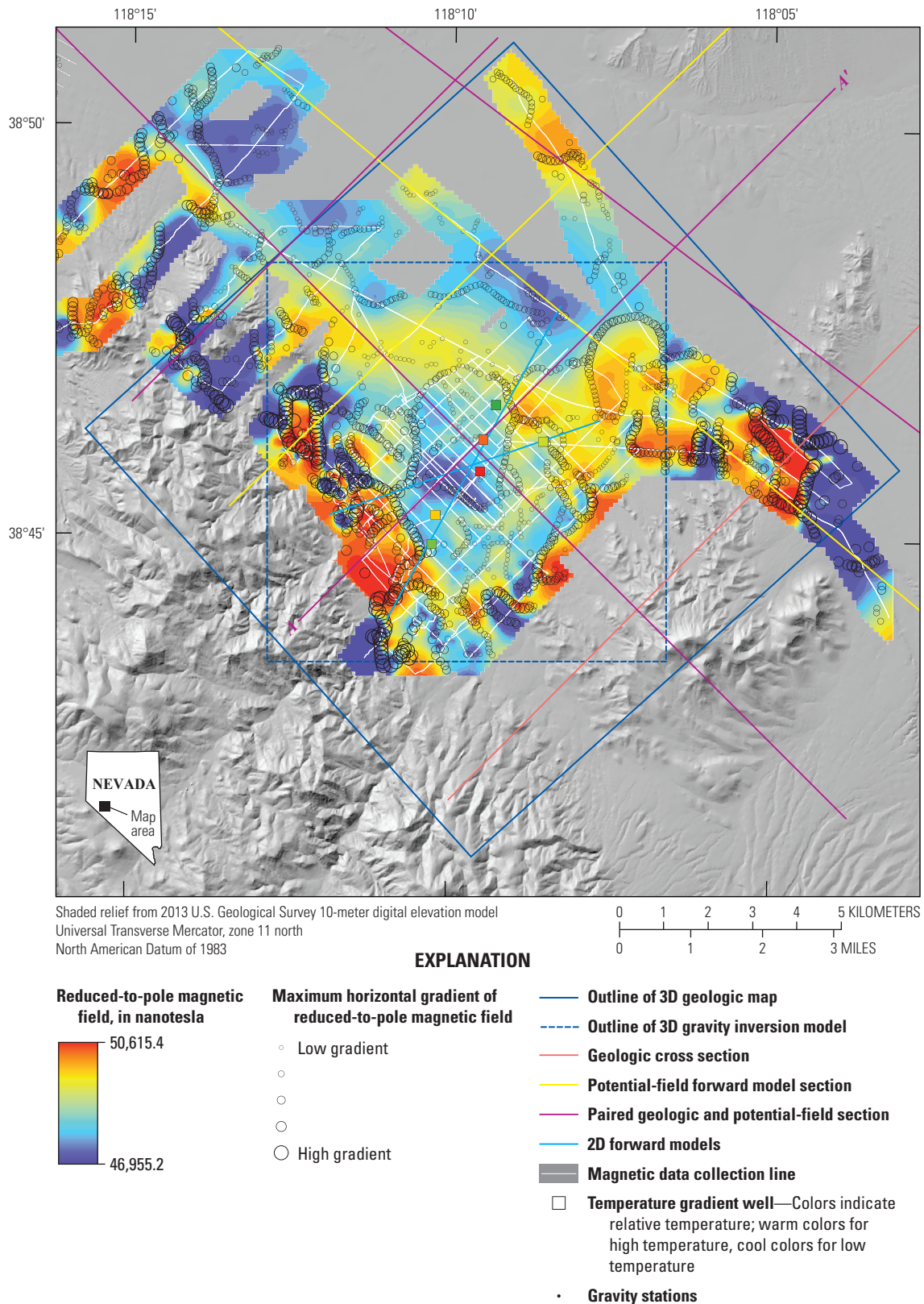
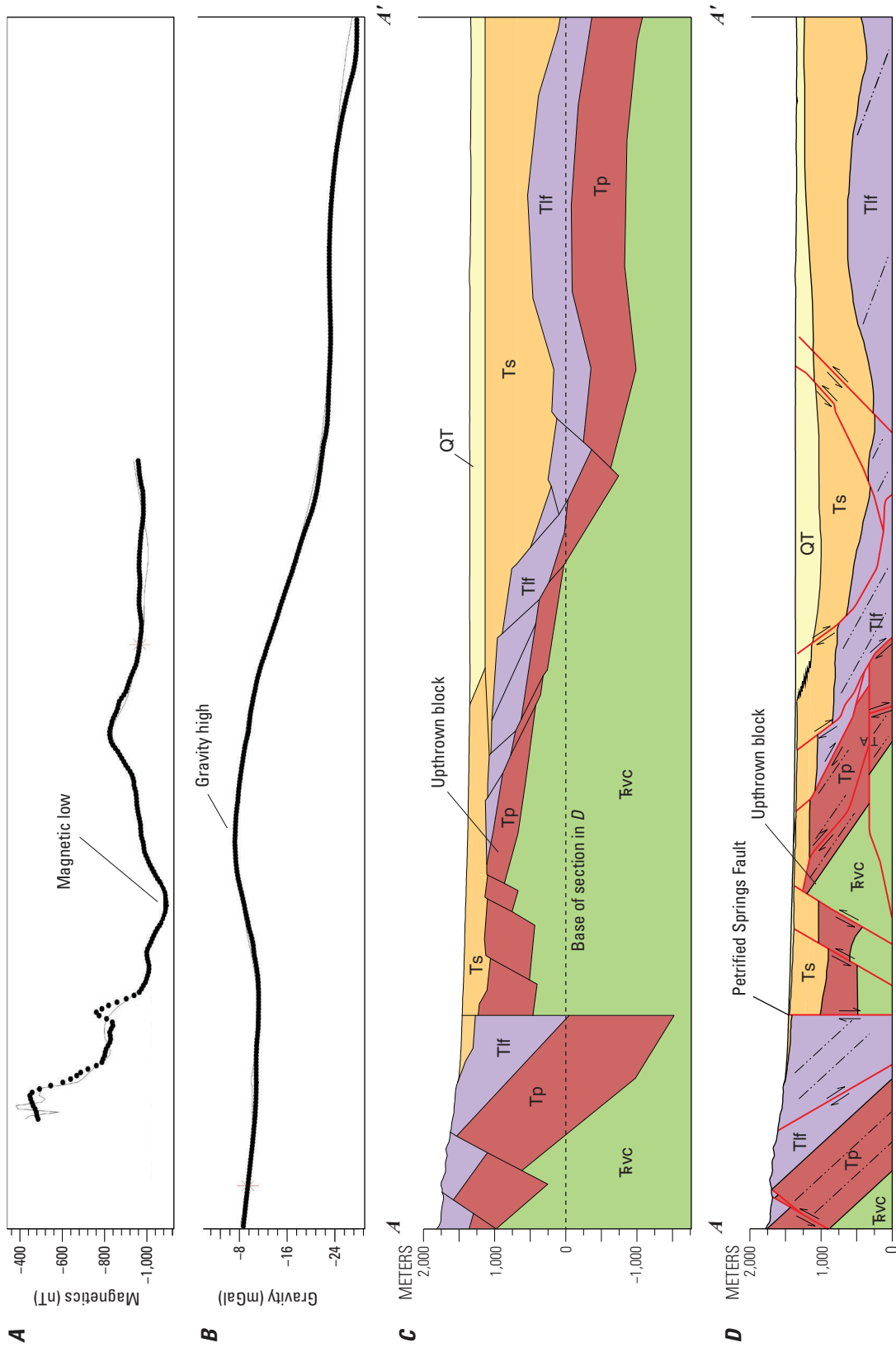


**Figure 4.** Map of reduced-to-pole magnetic field, magnetic data, and the locations of the maximum horizontal gradients in reduced-to-pole magnetics. Geologic cross sections and potential-field forward model sections used in construction of the 3D map are shown. Section A–A' shown on figure 5 is labeled. The locations of the temperature gradient wells drilled as part of this study are colored with respect to temperature, warm colors for high temperatures, cool colors for low temperatures; measured temperatures are shown on figure 2 (Faulds and others, 2018). 3D, three dimensional; 2D, two dimensional.



- EXPLANATION**
- QT Sediments and sedimentary rocks (Holocene to Miocene)
  - Ts Sediments and sedimentary rocks (Miocene)
  - Tlf Mafic to intermediate lavas of Mount Ferguson (Miocene)
  - Tp Poinsettia Tuff Member of the Hu-pwi Rhyodacite (Miocene)
  - RVC Metasedimentary and volcaniclastic rocks (Upper Triassic)
  - Normal fault (D) — Arrows indicate lateral offset
  - Geophysical block boundary (C)
  - Contact (D)
  - Dip of volcanic bedding (D)
  - Observed model value (A, B)
  - Calculated model value (A, B)

**Figure 5.** Potential-field forward models and geologic cross section for A–A' (fig. 1). A, Observed and calculated reduced-to-pole magnetic anomaly. B, Observed and calculated complete Bouguer gravity anomaly. C, Block model used to generate calculated gravity and magnetic anomalies in A and B; see table 1 for unit densities. D, Geologic cross section for A–A'. Geophysical models (A, B, and C) reproduced after Earney and others (2018). Geologic cross section (D) reproduced after Craig and others (2017), Craig (2018), and Craig and others (2021). No vertical exaggeration.

used this surface to define the top of basement rock (unit  $\overline{\text{FVC}}$ ). Other geologic geometries on the cross sections were informed by 1:24,000-scale geologic mapping (Craig, 2018). The six wells drilled as part of this study did not reach bedrock and provide no lithologic constraints.

For the 2D potential-field forward modeling, rock units from the initial geologic cross sections were assigned densities and magnetic susceptibilities on the basis of values determined from rock-property measurements, databases, and initial depth-to-basement modeling (table 1). Gravity and magnetic data were extracted from gravity and magnetic grids (figs. 3, 4). Magnetic remanences were used in the forward modeling only in units where magnetic remanence values were found to be relatively high compared to the total magnetic field. Geologic cross sections and forward models were adjusted together in a multi-step, iterative workflow where (1) geologic cross sections would inform initial forward model set up, (2) forward models would highlight necessary changes to geologic cross sections, and (3) the potential-field data were remodeled on the basis of new geologic geometries. The iterative workflow was repeated several times and allows geologic cross sections and potential field models to be iteratively adjusted, ensuring consistency with both geologic and geophysical data. An example of one paired geologic cross section and potential-field forward model along section line  $A-A'$  is shown in figure 5C and 5D

## 3D Geologic Mapping Methods

The southeastern Gabbs Valley geothermal area 3D geologic map was constructed using the methods summarized below. The methods described here are similar to those used in previous studies by Phelps and others (2008), Moeck and others (2010), Faulds and others (2010b), Jolie and others (2012, 2015), Hinz and others (2013), Siler and Faulds (2013), and Siler and others (2016a, b, 2019a, b). Commercial 3D software (Earthvision version 10, Dynamic Graphics Inc., Alameda, California) was used for all 3D mapping work. The 3D geologic map domain is 13 km by 13 km and extends from the land surface to 2,000 m below sea level. The 3D map domain is rotated 48° clockwise from north, such that the sides of the 3D volume are sub-parallel to the two dominant structural domains (fig. 2). The 3D fault system was constructed first, followed by the 3D stratigraphy and four rounds of 3D gravity inversion modeling were conducted to test and improve the fit between the gravity measurements and the 3D geology.

## 3D Fault Mapping

The 3D fault structure is based on faults defined by 1:24,000-scale mapping (fig. 2), geologic cross sections (fig. 5D; Craig and others, 2017; Craig, 2018; Craig and others, 2021), faults interpreted from gravity and magnetic anomalies and horizontal gradients (figs. 3, 4; Earney and others, 2018), and faults inferred from 2D forward modeling of the gravity and magnetic data (fig. 5A–5C; Earney and others, 2018). The final fault profiles from the cross sections and forward models, and

the surface fault traces were digitally added to the 3D software environment. A fault hierarchy, defining the cross-cutting relations among the faults, was built on the basis of the geologic map and cross sections. 3D fault surfaces were built from these input data using a minimum tension gridding algorithm provided within Earthvision software. Minimum tension gridding generates relatively smooth surfaces while conforming to the input data (Dynamic Graphics Inc., 2018; Johnson and Taylor, 2010). However, surfaces built using the minimum tension gridding algorithm might take on geologically unrealistic geometries in areas that lack constraining data. To mitigate this, the calculated fault surfaces were manually adjusted with additional constraints to guide the interpolation of the fault surfaces so they remain consistent with interpreted geologic relations. In other words, this step helps ensure that the strike, dip, and relative offset of faults, as constrained by the input data, were retained in the parts of the 3D map that have few measurements (for example, Siler and Faulds, 2013; Siler and others, 2016a, b; Siler and others, 2019a, b).

## 3D Stratigraphic Mapping

The 3D stratigraphic contacts were initially constructed on the basis of bedrock exposures mapped in the study area (fig. 2), geologic cross sections, and potential-field forward models (Craig and others, 2017; Craig, 2018; Earney and others, 2018; Craig and others, 2021; fig. 5). The southeastern Gabbs Valley area contains no subsurface geologic data; no wells, including those drilled as part of the project, reach bedrock. Many units from Craig and others (2017), Craig (2018), and Craig and others (2021) were lumped to simplify the subsurface stratigraphy to those units that could be reasonably projected to depth throughout the 3D domain (see “Description of Map Units” section for details). Additionally, 3D inversion modeling of gravity data was conducted to further constrain the 3D stratigraphy.

## 3D Gravity Inversion Modeling

The inversion modeling workflow used during four rounds of adjustment of the 3D geologic map is described below. SimPEG, an open-source geophysical code (Cockett and others, 2015) was used in conjunction with Rhino3D (version 7, Robert McNeel & Associates, Seattle, Washington) 3D design software for all 3D geophysical inversion modeling work. The methods used are similar to those detailed by Witter and others (2016).

The 3D gravity inversion domain for this study covers an 81 square kilometer (km<sup>2</sup>; 9 km by 9 km) domain extending from the land surface to 1,775 m below sea level. The inversion domain is located within the 3D geologic map area, though it does not fully cover the map area (figs. 2–4). This smaller area was selected because it contains the densest gravity station spacing. It is also small enough to be computationally manageable, though it covers the area of interest for this project: the displacement transfer zone and geothermal prospect. Cells within the model domain are cubes that are 50 m on a side, from the ground surface to a depth of 1,400 m. To make the geophysical inversion problem

more computationally tractable, we reduced the total number of model cells by increasing the size of the cells at deeper levels in the model volume. For depths between 1,400 and 2,475 m below ground surface, the model cells are 100 m on a side; below 2,475 m, the model cells are 200 m on a side. The total number of cells in the model is ~1.1 million. There are 472 gravity measurements at the ground surface within the model domain.

## Inversion Modeling Methods

The initial 3D geologic map consists of 5 stratigraphic units and 99 fault surfaces. From oldest to youngest, the stratigraphic units that constitute the 3D geologic map are: Late Triassic metasedimentary and volcanoclastic rocks (unit **Fvc**), Miocene Poinsettia Tuff Member of Hu-pwi Rhyodacite (unit **Tp**), Miocene mafic to intermediate lavas of Mount Ferguson (unit **Tlf**), and Holocene to Miocene sediments and sedimentary rocks (units **Ts** and **QT**; see “Description of Map Units” section for details). Gravity inversion modeling was conducted to evaluate the 3D geometry and spatial distribution of each unit and to minimize the difference between gravity measurements and calculated gravity response from modeled 3D stratigraphy. For 3D inversion modeling, only the geometry of stratigraphic contacts was changed, whereas the geometry and location of 3D faults remained unchanged. This simplification was made for two reasons: (1) the location and geometry of faults with large offsets are well constrained by potential-field forward models (fig. 5) and gravity and magnetic maximum horizontal gradients (figs. 3, 4), and therefore making adjustments to these faults was unlikely to meaningfully improve the geologic solution, and (2) allowing fault geometries to change would introduce unwanted variables when adjusting the 3D map based on the inversion results.

Four rounds of 3D gravity inversion were performed, each on the basis of a different version of the 3D geologic map (versions 1–4, referred to as V1, V2, V3, and V4 hereafter), with three separate inversions produced each round. The first two inversions in each round were (1) an inversion with a heterogeneous density distribution and no geologic constraints besides topography and (2) an inversion in which the topography and stratigraphic unit boundaries from the 3D map bound each stratigraphic volume in the inversion domain and with density values assigned to each volume and not allowed to change (table 1). These two inversions, though not likely to produce geologically meaningful results or match the gravity measurements, are performed as tests to explore the model space, gravity data, and density data.

The third inversion performed in each round is one in which the stratigraphic contacts from the 3D map constrain the stratigraphic volumes in the inversion domain and these volumes are inverted for a heterogeneous density distribution. V1–V4 inversions and the density models that are produced are discussed below and shown in figures 6–9. In these inversions, cells are assigned an initial density on the basis of the corresponding stratigraphic unit from the 3D map (table 1). As the inversion progresses, the inversion algorithm changes the density in each cell within geologically reasonable bounds, in our case  $\pm 500 \text{ kg/m}^3$ , from the initial density value. The inversion

algorithm (Cockett and other 2015) continues to modify the density value in each cell until the misfit between the gravity response from the density model and the observed complete Bouguer gravity anomaly is within the gravity measurement error (0.05 milligals [mGal]) for each of the 472 gravity measurements. The misfit at each gravity station for each of the four inversion rounds is shown on figure 6. Each inversion achieves a level of misfit that is less than 0.1 mGal at >95 percent of all gravity stations and less than 0.05 mGal at ~66 percent of all gravity stations (fig. 6). The standard deviation of the misfit for all gravity stations in each version ranges from 0.045 to 0.053 mGal for all density models produced in this study (fig. 6). This indicates that the inversion results match the observed gravity anomalies to within their uncertainty.

Although each density model is quantitatively consistent with gravity measurements, each is a non-unique solution and may not be geologically realistic. To evaluate whether the density models are geologically realistic, and to diagnose locations where the 3D geologic map could be changed to arrive at a more geologically meaningful solution, the 3D density model produced in each round of inversion is analyzed in three ways: (1) the calculated density values in each stratigraphic unit are checked to ensure that they are reasonable for that rock type, (2) the spatial distribution of density within each stratigraphic unit is visually analyzed to determine if changes to the position of stratigraphic surfaces are needed, and (3) the statistical distribution of density values is analyzed to evaluate the homogeneity of density in each stratigraphic unit. In making these adjustments, we assume that a more homogeneous density distribution within each stratigraphic unit corresponds with a more geologically realistic 3D geologic map. This assumption ignores the possibility that intra-unit density heterogeneity may exist for geologically realistic reasons. Possible reasons for density heterogeneity include silicification, other alteration, or unmapped intrusions. In addition, intra-unit density variability associated with lateral or vertical lithologic variation caused by channelization or other geomorphic, volcanic, or tectonic processes could affect all rocks in the subsurface. Though each of these scenarios involving intra-unit density variability is possible in the study area, the objective of building the 3D geologic map was to construct an accurate representation of the subsurface to facilitate further assessment of the subsurface and geological hydrothermal system in southeastern Gabbs Valley. The methods and assumptions we employed ensure that the 3D geologic map is consistent with all the input data. Though it is simplified, the map serves as a baseline representation of the geologic architecture that can be updated with additional complexity as new data are collected. The methods used for adjustments to the 3D geologic map as a result of each round of inversion are detailed below.

## Adjustment of the 3D Map Based on Inversion Results

Figures 7, 8, and 9 show the inversion results for each round of gravity inversion modeling. Figure 7 shows a slice along section *B–B'* (section line shown on fig. 2) through the 3D density model produced in each of the four rounds. Figure

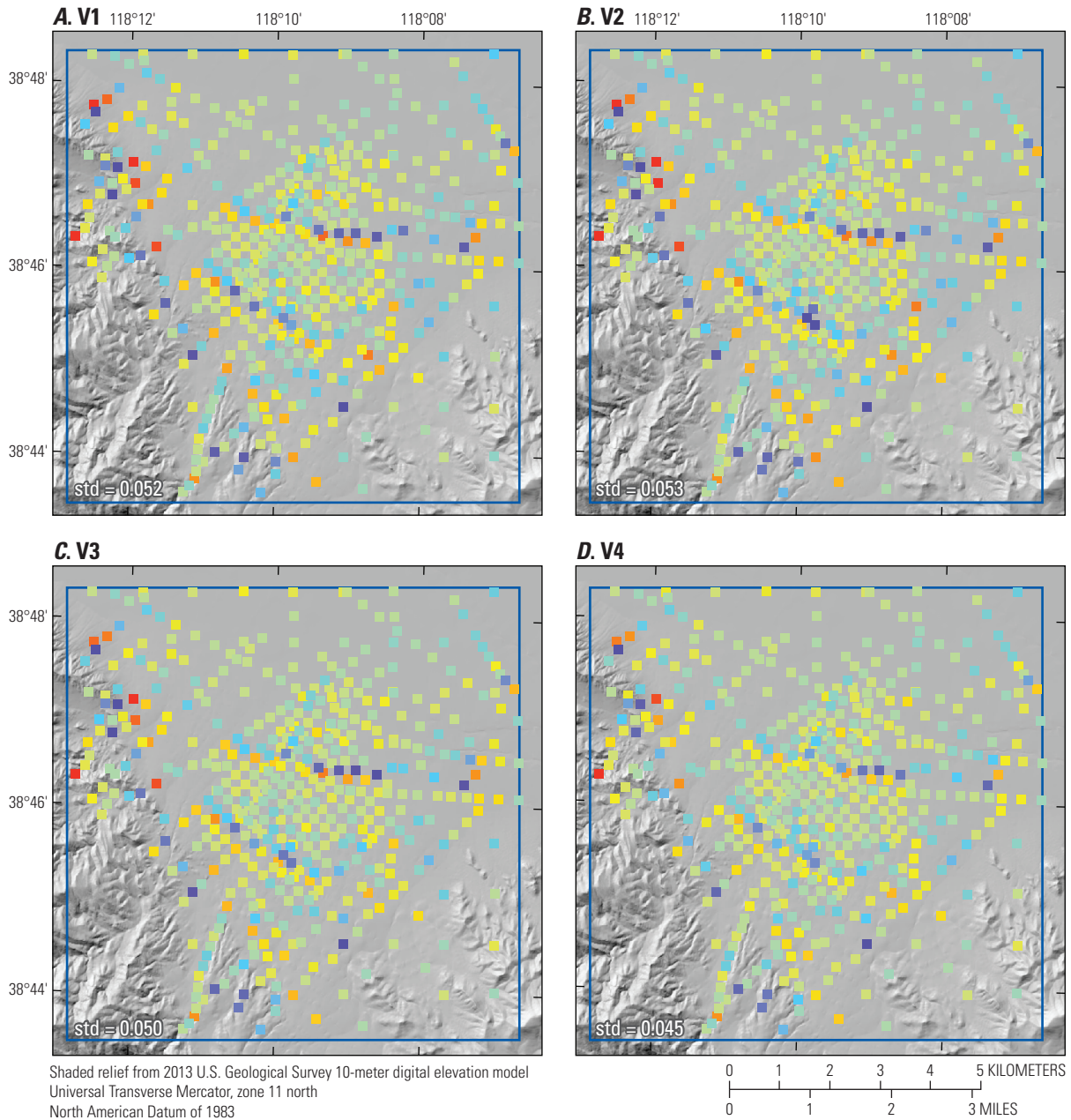
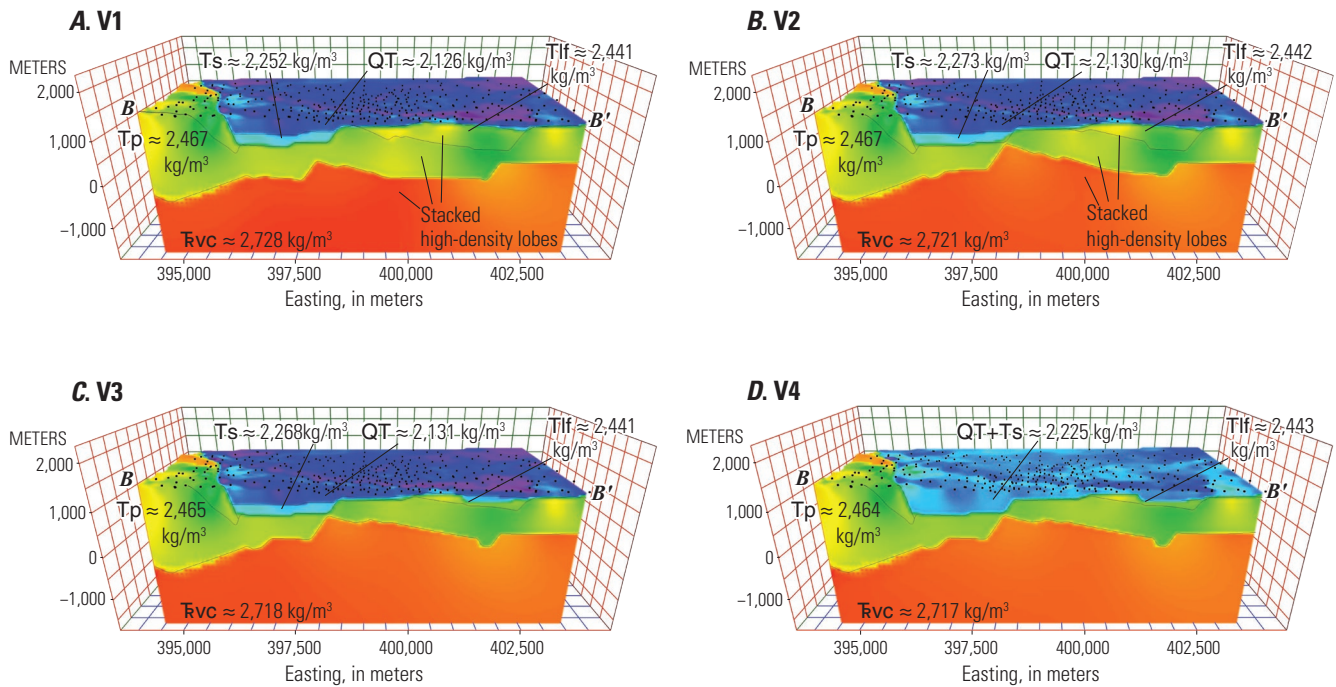
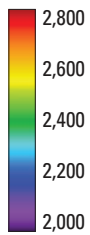


**Figure 6.** Maps of misfit between the observed complete Bouguer gravity anomaly and calculated gravity for the four gravity inversions (version 1–4, or V1, V2, V3, V4) at the 472 gravity stations within the inversion model area. *A*, V1. *B*, V2. *C*, V3. *D*, V4. Warm and cool colors indicate relatively higher misfit, whereas neutral colors (green) indicated lower misfit. The standard deviation (std) of the misfits in milligals (mGal) for all gravity stations are shown on each map. 3D, three dimensional.



### EXPLANATION

Density, in kilograms per cubic meter (kg/m<sup>3</sup>)



### Stratigraphic unit abbreviation

QT	Sediments and sedimentary rocks (Holocene to Miocene)
Ts	Sediments and sedimentary rocks (Miocene)
Tlf	Mafic to intermediate lavas of Mount Ferguson (Miocene)
Tp	Poinsettia Tuff Member of the Hu-pwi Rhyodacite (Miocene)
Fvc	Metasedimentary and volcanoclastic rocks (Upper Triassic)

8 shows densities greater than or equal to 2,550 kg/m<sup>3</sup> for each density model, values generally expected for basement rocks (described in the “Description of Map Units” section). Figure 9 shows histograms of the density values in each stratigraphic unit for each density model. Table 2 reports the median, standard deviation, interquartile range of density values in each stratigraphic unit for each round of inversion, and the differences in standard deviations and interquartile ranges between each round of inversions.

## Round 1—The Initial 3D Geologic Map and Density Model

The initial (V1) 3D geologic map was built based on preliminary versions of the geologic cross sections and potential-field forward models (Craig and others, 2017; Craig, 2018; Earney and others, 2018; Craig and others, 2021). During construction of the V1 3D map, it became clear that the geologic cross sections and geophysical forward models were inconsistent with one another in some parts of the model domain. As a result, four sections were selected for iterative adjustments to maximize the agreement between geological and geophysical observations, as described above. After the iterative adjustments

**Figure 7.** Three-dimensional (3D) density models for each round of gravity inversion modeling (versions 1–4, or V1–V4), oblique view looking north sliced along cross section B–B’ (location shown in fig. 2). A, V1. B, V2. C, V3. D, V4. The 3D stratigraphic surfaces from each version of the 3D map are shown as faint black lines on the sliced face of the 3D volume. The listed densities are the median for each stratigraphic unit (table 2 and fig. 9). kg/m<sup>3</sup>, kilogram per cubic meter.

and completion of the V1 3D geologic map, gravity inversion modeling was performed based on the V1 stratigraphic surfaces.

Certain characteristics of the V1 3D density model produced by gravity inversion indicate possible improvements to the 3D geologic map. Within each stratigraphic unit there are several discrete high- and low-density lobes that contrast with the density of the rocks within the same stratigraphic unit. This includes a set of vertically stacked relatively dense lobes, one each for Late Triassic metasedimentary and volcanoclastic rocks, Miocene Poinsettia Tuff Member of Hu-pwi Rhyodacite, Miocene mafic to intermediate lavas of Mount Ferguson (units Fvc, Tp, and Tlf, respectively; fig. 7A), and a high-density lobe ( $\geq 2,550$  kg/m<sup>3</sup>) above the unit Fvc stratigraphic surface in the approximate center of the density model (fig. 8A).

We consider two possible explanations for these observations: (1) the geologic units in question have relatively high- or low-density areas or (2) the stratigraphic surfaces are in the wrong locations; therefore, unrealistically high- or low-density rocks are needed to fit the gravity measurements. There are geologically realistic explanations for both. As described above, discrete areas of the subsurface with locally high- or low-density rocks are possible in the study area. For this exercise however, we assume that these are lobes of “anomalous” density

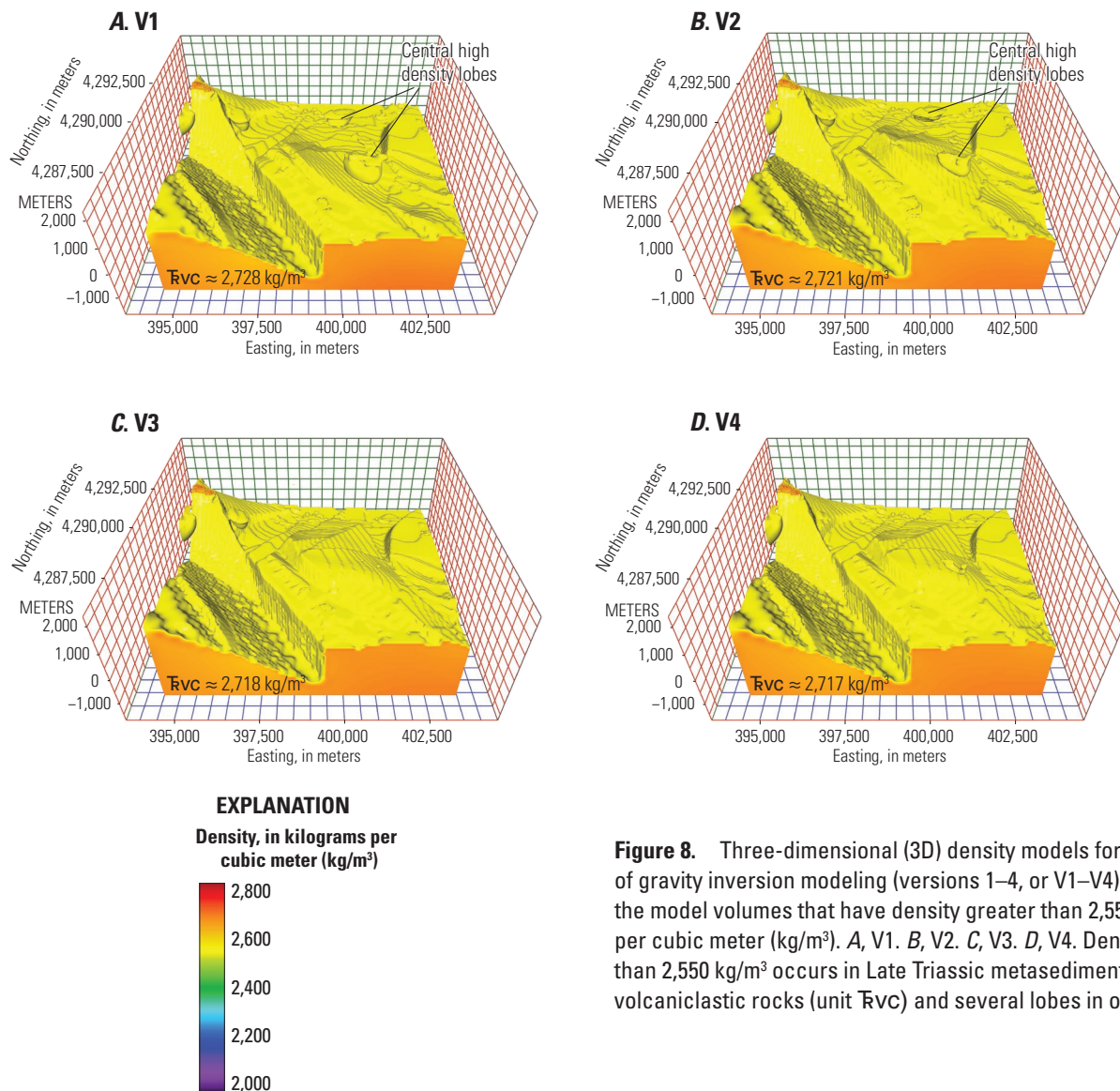


**Figure 8.** Three-dimensional (3D) density models for each round of gravity inversion modeling (versions 1–4, or V1–V4), showing the model volumes that have density greater than 2,550 kilograms per cubic meter ( $\text{kg}/\text{m}^3$ ). *A, V1. B, V2. C, V3. D, V4.* Density greater than 2,550  $\text{kg}/\text{m}^3$  occurs in Late Triassic metasedimentary and volcaniclastic rocks (unit  $\bar{\rho}_{vc}$ ) and several lobes in overlying units.

and indicate changes that need to be made to the position of the 3D stratigraphic surfaces. As explained above, we contend that the most geologically realistic and meaningful stratigraphic models will maximize homogeneity in density within individual stratigraphic units while retaining low misfit between observed and calculated gravity values. The steps taken to evaluate the intra-unit density homogeneity include (1) visual inspection of the size, location, and density of the anomalous density lobes (figs. 7, 8) and (2) analysis of the distribution, standard deviations, and interquartile ranges of the density in each stratigraphic unit (fig. 9, table 2).

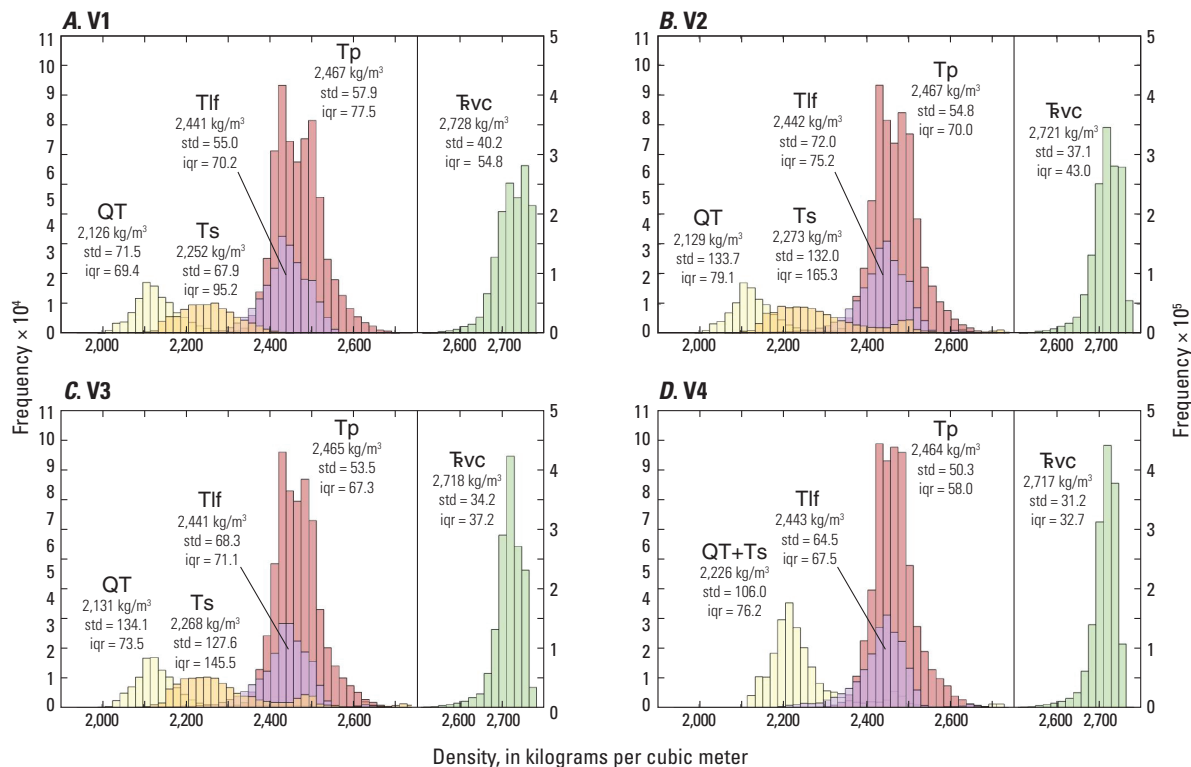
## Round 2—Version 2 Geologic Map and Density Model

The V2 3D geologic map was adjusted from the V1 map to remove the anomalous density lobes that occur in each stratigraphic unit (figs. 7A, 8A), and thus increase intra-unit density homogeneity. To produce the V2 map, the four paired

geologic cross sections and geophysical forward model profiles were iteratively adjusted for consistency. The changes to the 3D stratigraphic surfaces were made along these new 2D cross sections (for example, fig. 5). Though stratigraphic adjustments along the 2D cross sections naturally resulted in some small, off-section changes, the most substantial adjustments occurred along the section profiles, so the changes made between the V1 and V2 3D geologic maps were essentially 2D changes. The faults remained unchanged. The V2 density model (figs. 7B, 8B, 9B) was produced on the basis of the above inversion methods and the V2 3D stratigraphic surfaces. These changes did not remove the stacked high-density lobes (compare fig. 7A to 7B) or the central high-density lobe (compare fig. 8A to 8B).

## Round 3—Version 3 Geologic Map and Density Model

The V3 3D geologic map was produced by altering the V2 map on the basis of the anomalous density lobe locations in



#### EXPLANATION

- QT Sediments and sedimentary rocks (Holocene to Miocene)
- Ts Sediments and sedimentary rocks (Miocene)
- Tlf Mafic to intermediate lavas of Mount Ferguson (Miocene)
- Tp Poinsettia Tuff Member of the Hu-pwi Rhyodacite (Miocene)
- Tvc Metasedimentary and volcanoclastic rocks (Upper Triassic)

**Figure 9.** Histograms of density distributions in each stratigraphic unit for each round of gravity inversion modeling (versions 1–4, or V1–V4). The median densities, standard deviations (std), and interquartile range (iqr) are labeled for each unit and are also listed in table 2. A, V1. B, V2. C, V3. D, V4. Note that histograms for Late Triassic metasedimentary and volcanoclastic rocks (unit Tvc; green) have different axes and scales from the histograms for the other units. kg/m<sup>3</sup>, kilogram per cubic meter.

the V2 density model in three dimensions, rather than making alterations strictly along section lines. In areas where there was a high-density lobe, the nearest stratigraphic surface(s) were moved shallower (to bring deeper, denser rocks closer to the ground surface), and in areas where there was a low-density lobe, the nearest stratigraphic surface(s) were moved deeper (to increase the thickness of shallower, less-dense rocks). In general, elevation changes were on the order of tens to hundreds of meters. As changes were made to the 3D geologic map, “difference surfaces”—the elevation of the V2 stratigraphic surface subtracted from the same surface in V3—were calculated (fig. 10). This process ensured that changes to the stratigraphic surfaces were made only in locations that have observed anomalous density and not elsewhere. Although no changes to fault geometries were made, stratigraphic offsets across faults did change where stratigraphic contacts were altered.

## Round 4—Version 4 Geologic Map and Density Model

The V4 3D geologic map was produced by lumping Holocene to Miocene sediments and sedimentary rocks (units QT and Ts) into a single unit, QT+Ts; no other changes were made. Unit QT and unit Ts were originally mapped separately in V1, V2, and V3 because unit Ts is a distinctive mappable unit in the Gabbs Valley area. It is dominated by the late Miocene Esmeralda Formation consisting largely of tuffaceous lacustrine deposits, and thus is distinctive from unit QT (Ekren and others, 1980; Ekren and Byers, 1985, 1986a, b; Craig 2018; see “Description of Map Units” section for details). In analyzing the V3 results however, we acknowledge that the 3D stratigraphic surface between units QT and Ts is probably the least well constrained of the stratigraphic surfaces. Though exposed in the study area

**Table 2.** Calculated density model results for four three-dimensional gravity inversions (versions 1–4).

[Values in kilograms per cubic meter. Differences between versions are shown; negative values indicate a smaller value than the previous version and an increase in density homogeneity in the subsequent version. Units QT and Ts, Holocene to Miocene sediments and sedimentary rocks; unit Tlf, Miocene mafic to intermediate lavas of Mount Ferguson; unit Tp, Miocene Poinsettia Tuff Member of the Hu-pwi Rhyodacite; unit  $\bar{\text{Tvc}}$ , Late Triassic metasedimentary and volcanoclastic rocks. SD, standard deviation; IQR, interquartile range; —, no data]

**A.** Model results for version 1 (V1).

Geologic map unit label	Median	SD	IQR
QT	2,126	71.5	69.4
Ts	2,252	67.9	95.2
Tlf	2,441	55.0	70.2
Tp	2,467	57.9	77.5
$\bar{\text{Tvc}}$	2,728	40.2	54.8

**B.** Model results for version 2 (V2).

Geologic map unit label	Median	SD	IQR	V2–V1 SD change	V2–V1 IQR change
QT	2,129	133.7	79.1	62.2	9.7
Ts	2,273	132	165.3	64.1	70.1
Tlf	2,442	72	75.2	17	5
Tp	2,467	54.8	70	–3.1	–7.5
$\bar{\text{Tvc}}$	2,721	37.1	43	–3.1	–11.8

**C.** Model results for version 3 (V3).

Geologic map unit label	Median	SD	IQR	V3–V2 SD change	V3–V2 IQR change	V3–V1 SD change	V3–V1 IQR change
QT	2,131	134.1	73.5	0.4	–5.6	62.6	4.1
Ts	2,268	127.6	145.5	–4.4	–19.8	59.7	50.3
Tlf	2,441	68.3	71.7	–3.7	–3.5	13.3	1.5
Tp	2,465	53.5	67.3	–1.3	–2.7	–4.4	–10.2
$\bar{\text{Tvc}}$	2,718	34.2	37.2	–2.9	–5.8	–6	–17.6

**D.** Model results for version 4 (V4).

Geologic map unit label	Median	SD	IQR	V4–V3 SD change	V4–V3 IQR change	V4–V2 SD change	V4–V2 IQR change	V4–V1 SD change	V4–V1 IQR change
QT+Ts	2,226	106	76.2	—	—	—	—	—	—
Tlf	2,443	64.5	67.5	–3.8	–4.2	–7.5	–7.7	9.5	–2.7
Tp	2,464	50.3	58	–3.2	–9.3	–4.5	–12	–7.6	–19.5
$\bar{\text{Tvc}}$	2,717	31.2	32.7	–3	–4.5	–5.9	–10.3	–9	–22.1

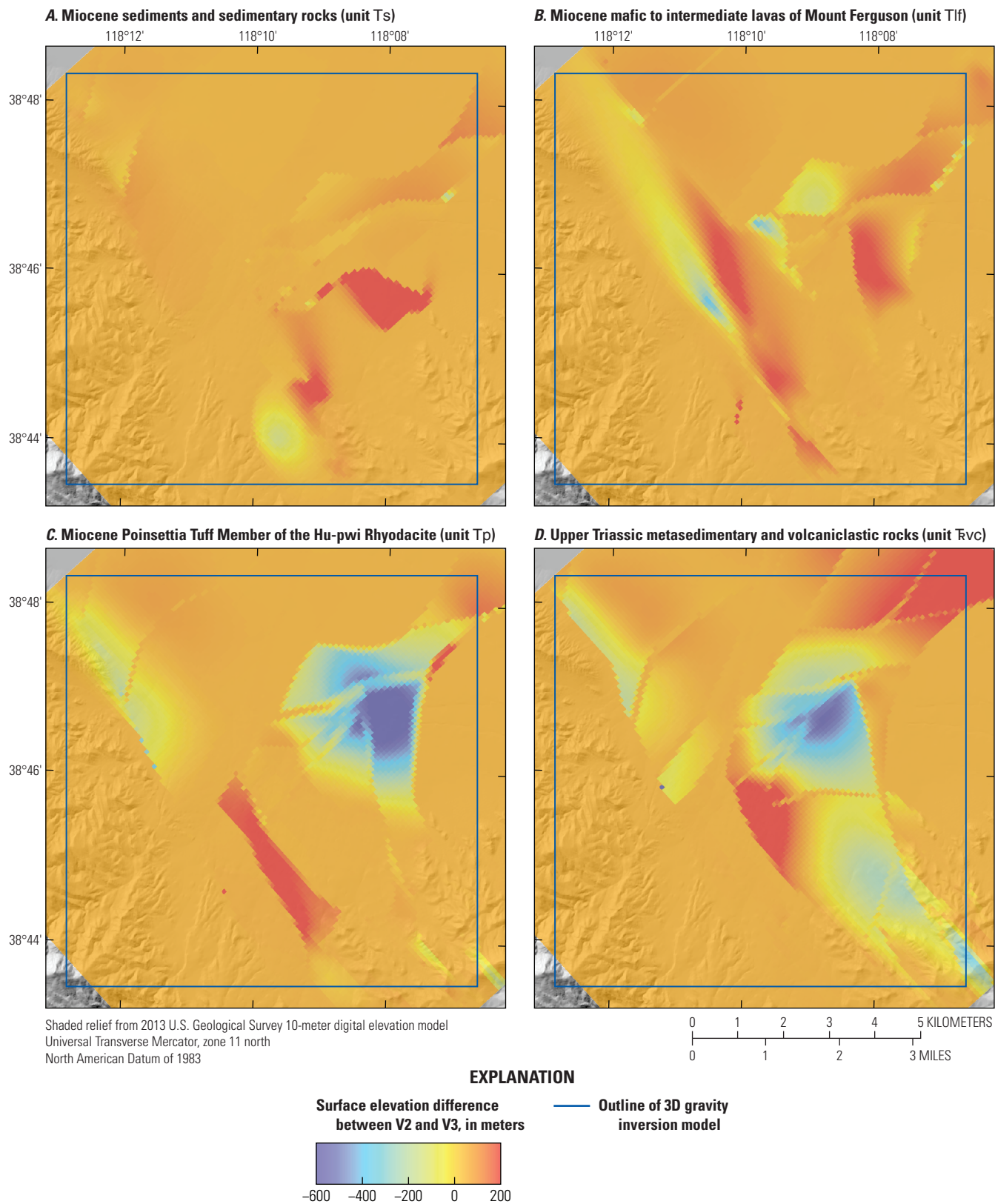


**Figure 10.** Maps of surface elevation differences—the difference in elevation between version 2 (V2) and version 3 (V3) for the top surface of each of the four stratigraphic units altered during adjustments to the map based on three-dimensional (3D) gravity inversion modeling. *A*, Miocene sediments and sedimentary rocks (unit Ts). *B*, Miocene mafic to intermediate lavas of Mount Ferguson (unit Tlf). *C*, Miocene Poinsettia Tuff Member of Hu-pwi Rhyodacite (unit Tp). *D*, Late Triassic metasedimentary and volcanoclastic rocks (unit Tvc). Cooler colors indicate that the V3 stratigraphic surface is shallower than the V2 surface, warmer colors indicate that the V3 stratigraphic surface is deeper than the V2 surface.

(fig. 2; Craig and others, 2017; Craig, 2018; Craig and others, 2021), the area of the unit QT and Ts contact exposure is relatively small compared to the other contacts. Additionally, though the surface is informed by 2D potential-field modeling and the densities and susceptibilities used in the modeling are appropriate for the rock types, no field measurements support these values for units QT and Ts (table 1). This means the thickness and lateral continuity of unit Ts, and therefore the stratigraphic contact between units QT and Ts throughout the study area, are not well constrained. To arrive at a more meaningful geologic solution, a fourth version (V4) of the 3D map was produced by combining units QT and Ts into a single unit.

For the V4 gravity inversion, unit QT+Ts has a starting density of 2,165 kg/m<sup>3</sup>, the mean of the starting density values for units QT and Ts (table 1). The V4 density model (figs. 7D, 8D, and 9D) was produced based on the methods described in the “3D Gravity Inversion Modeling” section and the V4 stratigraphic surfaces.

## Comparison of the Density Inversion Models

If our stated assumption of maximized density homogeneity is valid, the progressive removal of discrete anomalous density lobes and narrowing of the density range within each geologic unit toward a median value with a low standard deviation and interquartile range represent improvements toward capturing a more accurate representation of the subsurface.

The calculated gravity response in all four density models fits the gravity measurements within the 0.05 mGal uncertainty (fig. 6). Additionally, all four density models have median densities for Late Triassic metasedimentary and volcanoclastic rocks, Miocene Poinsettia Tuff Member of Hu-pwi Rhyodacite, Miocene mafic to intermediate lavas of Mount Ferguson (units FVC, Tp, and Tlf, respectively) that are consistent with density measurements (tables 1, 2). There are no density measurements from field samples to validate the densities of Holocene to Miocene sediments and sedimentary rocks (units QT, Ts, and the combined unit QT+Ts), though the modeled densities are reasonable for Quaternary and Tertiary sediments and sedimentary rocks (Ponce, 2021). Comparing the V1 and V2 models, the stacked high-density lobes in V2 appear to be more similar to the mean density of the unit and smaller than in V1 (compare figure 7A to 7B), though the central high-density lobes in V2 appear to be unchanged or even marginally larger relative to V1 (compare fig. 8A to 8B). Although the standard deviations and interquartile ranges for units FVC and Tp are lower in V2

than V1, the standard deviations and interquartile ranges for units QT, Ts, and Tlf are all higher in V2 than V1 (compare fig. 9A to 9B; table 2). Although these results are somewhat conflicting, densities in each unit in V2 are not more homogenous than they are in V1, so we infer that V2 is not a more geologically realistic solution relative to V1.

Visual analysis indicates that, compared to the V1 and V2 density models, the V3 and V4 density models have fewer anomalous density lobes. The anomalous density lobes that do exist in the V3 and V4 models are smaller and have densities that are closer to the median for each unit relative to the V1 and V2 models. For example, the stacked high-density anomalies in the V1 and V2 models (fig. 7A, B) are not evident in the V3 and V4 models (fig. 7C, D), and the multiple central high-density lobes in V1 and V2 (fig. 8A, B) are absent in V3 and reduced to one relatively smaller lobe in V4 (fig. 8C, 8D). Generally, anomalous density lobes appear to be less prevalent in V4 (fig. 9D), though some occur at the edges of the inversion model, potentially caused by sparse gravity measurements at the edge of the study area.

The histograms for units FVC, Tp, and Tlf become progressively narrower from V1 to V4, indicating that density values are nearer to the median for these units. Accordingly, the standard deviations and interquartile ranges for units FVC and Tp are progressively lower from V1 to V4 (compare fig. 9A–B to 9D–C; table 2). The standard deviations and interquartile ranges for unit Tlf also become progressively lower from V1 to V4, but with some exceptions. For V3, standard deviation and interquartile range of unit Tlf is lower relative to V2, but higher relative to V1. For V4, standard deviation and interquartile ranges of unit Tlf are lower relative to all previous versions, with the exception of the higher standard deviation of V1 compared to V4. Throughout the inversion modeling process, the density homogeneity largely increased for the three bedrock units (units FVC, Tp, and Tlf). Further density measurements would improve measured density distribution in each unit improving evaluation of whether the modeled densities and ranges are appropriate.

Given our stated intent of maximizing intra-unit density homogeneity, both the V3 and V4 density models appear to be more geologically realistic solutions compared to V1 or V2. The combination of units QT and Ts into unit QT+Ts, the only change made between V3 and V4, resulted in increased homogeneity in the underlying bedrock units, likely owing to the removal of a poorly constrained density boundary in the shallow units. Given our preference to generate a model with minimal intra-unit heterogeneity and the above stated limitations of distinguishing units QT and Ts in 3D, we conclude that V4 is the most geologically realistic solution of the four models. The final 3D geologic map described below and shown on the map sheet is the V4 3D geologic map with a combined QT+Ts unit.

## Structure of the 3D Geologic Map

The 3D map consists of 99 fault surfaces. There are two late Miocene–Quaternary structural domains described in the map: (1) northwest striking, sub-vertical, dextral strike-slip faults and steeply dipping dextral normal faults and (2) east–northeast to northeast striking, steeply dipping normal faults (fig. 1; Craig and others, 2017; Craig, 2018; Craig and others, 2021). Structure in the 3D map is dominated by an upthrown block located at the intersection zone between west-northwest striking dextral and dextral-normal faults, including the Petrified Spring Fault, and the northeast and east-northeast striking normal faults. The upthrown block is evident on section *A–A'* (fig. 5) and as a gravity high in the approximate center of the map (fig. 3). At the southwestern margin of the upthrown block is a dense fault intersection zone where dextral displacement along the Petrified Springs Fault and other strike-slip faults is transferred to dip-slip displacement on northeast and east-northeast striking normal faults.

## Stratigraphy of the 3D Geologic Map

After iterative 3D gravity inversion adjustments, the final 3D map consists of four geologic units: Holocene to Miocene sediments and sedimentary rocks (unit QT+Ts), Miocene mafic to intermediate lavas of Mount Ferguson (unit Tlf), Miocene Poinsettia Tuff Member of the Hu-pwi Rhyodacite (unit Tp), and Late Triassic metasedimentary and volcanoclastic rocks (unit Tvc). These lumped groups of units are either described by or modified from units described by Ekren and others (1980), Ekren and Byers (1985, 1986a, b), and Craig (2018); see “Description of Map Units” section.

## The Southeastern Gabbs Valley Geothermal System

The motivation for constructing this 3D geologic map was to aid in assessment of unknown hydrothermal resources in southeastern Gabbs Valley. The subsurface geologic geometries defined by this map, and the associated geologic and geophysical analysis, help inform the location and controls of hydrothermal activity. The 3D geologic map constrains the location and geometry of an upthrown block (fig. 5C, 5D) at the displacement transfer zone, where dextral strike-slip motion along the Petrified Springs Fault is transferred to normal slip along the northeast and north-northeast striking faults (fig. 2). At the location of the upthrown block and displacement transfer zone, a gravity high (figs. 3, 5B) occurs collocated with a magnetic low (figs. 4, 5A). A magnetic low is not expected here since Miocene mafic to intermediate lavas of Mount Ferguson and Miocene Poinsettia Tuff Member of Hu-pwi Rhyodacite have relatively high magnetic susceptibilities (table 1) and are relatively close to the surface (fig. 5). The magnetic low is interpreted as an area where the shallow volcanic units have been demagnetized owing to hydrothermal alteration (for example, Bouligand and others 2014). The zone of fault intersection, gravity high, and inferred demagnetized rocks is also collocated with a shallow (less than

50 m), dome-shaped, low electrical resistivity (<10 ohm meter) feature evident from magnetotelluric data (Peacock and others, 2018). This feature is likely a clay cap caused by hydrothermal alteration of the normally high resistivity volcanic rocks to relatively low resistivity (and therefore electrically conductive) illite and (or) smectite clays (for example, Munoz, 2014).

To investigate the multiple indications of shallow hydrothermal activity and test the above interpretations of hydrothermal processes, six 150-m-deep temperature gradient wells were drilled across the study area. Hydrothermal fluids with temperatures of 114.5 °C and 124.9 °C were encountered in two temperature gradient wells (fig. 2; Craig and others, 2017; Faulds and others, 2018; Craig and others, 2021). These temperatures are within the range of the fluid temperatures in developed geothermal fields in the Great Basin region (Ayling, 2020). Relatively lower temperatures (29 °C and 47.6 °C) were encountered in the wells to the north and south, respectively (fig. 2). These data, coupled with the structural interpretations from the 3D geologic map indicate hydrothermal fluids rise from depth along intersecting faults bounding the upthrown block. There is no expression of hydrothermal fluids at the surface, so the hydrothermal fluids likely outflow and disperse into shallow Holocene to Miocene sediments and sedimentary rocks (unit QT+Ts). These fluids, possibly mixed with shallow groundwater, were those encountered by the temperature gradient wells. Which specific fault(s) or segments of faults transmit the upwelling from depth remains unclear. For additional analyses of the southeastern Gabbs Valley geothermal system including conceptual models and power capacity estimates see Craig and others, 2021.

## Potential Applications for the 3D Geologic Map

### Conventional Geothermal Research and Resource Assessment

U.S. Department of Energy and U.S. Geological Survey resource assessments indicate that a more than five-fold increase in electricity production is possible from conventional hydrothermal resources in the United States (Williams and others, 2007, 2008, 2009; Hamm and others, 2019). Much of the untapped resource base likely lies in blind hydrothermal systems—those with no surface expression (Coolbaugh and others, 2007)—like the newly recognized southeastern Gabbs Valley system. The drilling campaign that encountered the 114.5 °C and 124.9 °C hydrothermal fluids at ~150 m depth was guided by data used in the construction of the 3D geologic map and the subsurface geologic geometries described therein. The successful drilling campaign demonstrates the utility of these data and 3D geologic maps in characterization and assessment of geothermal resources. 3D geologic maps, like the southeastern Gabbs Valley map developed in this study, may form the basis for testable conceptual models of hydrothermal processes, aiding resource assessment and development, for example Craig and others (2021).

## Reservoir Modeling and Management

Generation of electricity from hydrothermal systems requires production of hot fluid or steam and injection of fluid back into the subsurface. Management of production and reinjection is a complex balance of maintaining pressure in the geothermal reservoir through reinjection, while minimizing the temperature decline that can occur as a result of injecting cooler fluids into the hotter hydrothermal system. Accurate representations of subsurface geologic features, like those depicted in 3D geologic maps, can help constrain crucial numerical model parameters of reservoirs such as porosity, permeability, and spatial distribution, and contribute to better resource management (for example, Milicich and others, 2018).

## Seismic Hazard Analysis

Gabbs Valley is an area crossed by historically active faults that represent a natural seismic hazard for local communities. There have been several historical, relatively large earthquakes associated with Walker Lane and Basin and Range faults within and adjacent to Gabbs Valley. Surface ruptures associated with the magnitude (*M*) 7.2 1932 Cedar Mountain earthquake extend into the 3D geologic map area (fig. 2; Bell and others, 1999). A sequence of thousands of earthquakes as large as *M*4.8, occurred throughout 2011 (Zha and others, 2019) near the city of Hawthorne, Nevada, ~40 km west-southwest of the map area (fig. 1). The *M*6.5 May 15, 2020, Monte Cristo Range earthquake occurred ~70 km south of the map area (fig. 1; Zheng and others, 2020). 3D geologic maps provide data including fault orientations, lengths, offsets, and spatial distribution, which can be paired with local seismicity data and the location of sensitive infrastructure to evaluate the hazard associated with natural seismicity in the area (for example, Kaven and others, 2019).

## Basin Hydrogeology

Groundwater resources associated with both agricultural irrigation and drinking water are critical to the sustainability of many private and public interests in arid parts of the western United States, including Gabbs Valley. Though the fluid

chemistry in the southern Gabbs Valley hydrothermal system is not well constrained, geothermal fluids can, in some cases, be unsuitable for these purposes owing to high temperatures, salinity, or water chemistry. However, Basin and Range hydrothermal systems typically have a relatively small footprint of <10 km<sup>2</sup> (Wilmarth and Stimac, 2015). Within the 3D geologic map area, but distinct from the hydrothermal system, ambient temperature groundwater may be suitable for agriculture or drinking water. 3D geologic maps provide information that is applicable to the assessment and management of water resources in the map area. The faults and basin structure shown in the map control the distribution of sedimentary and volcanic rocks and both can be important aquifers (for example, Glancy, 1986; Maurer and Welch, 2001).

## Education and Scientific Inquiry

Interactive 3D geologic maps offer users a powerful tool for visualizing geologic features from various perspectives and exploring these features at depth. Slices through the map can illustrate geologic relations along cross sections of any orientation. This 3D geologic map of southeastern Gabbs Valley helps to visualize the complex spatial relations generated by faulting, folding, erosion, sedimentation, and other geologic processes more quickly and easily than a 2D map would. In this way, 3D geologic maps are a useful interpretive and teaching tool that enhance the information provided in 2D geologic maps by allowing the user to more readily visualize complex geologic features.

## Acknowledgments

This project was funded by a U.S. Department of Energy grant (the Nevada Play Fairway Project) awarded to James E. Faulds (grant number DE-EE0006731), by the Mendenhall Program of the U.S. Geological Survey, and by the Geothermal Resources Investigation Project funded by the Energy Resources Program of U.S. Geological Survey. Reviews by Daniel Scheirer and Michelle Roberts significantly improved the pamphlet and the map sheet.

## DESCRIPTION OF MAP UNITS

### SEDIMENTARY DEPOSITS

**QT+Ts Sediments and sedimentary rocks (Holocene to Miocene)**—Dominated by sedimentary rocks, includes minor basalt, tuffs, and tuffaceous sedimentary rocks. Unit consists of both units QT and Ts, separate units in versions 1–3 of the 3D map, lumped together in final version shown on map sheet. Unit QT consists of alluvium (Qa, Qai, Qay), eolian deposits (Qe), alluvial fan deposits (Qfi, Qfo, Qfy, QTf) from Craig (2018) and playa deposits (Qp) and eolian deposits (Qs) from Ekren and others (1980) and Ekren and Byers (1985, 1986a, b). Unit Ts consists of basalt (Tb), pebble conglomerate (Tcg), Esmeralda Formation (Te), and eolian deposits (Tes) from Craig (2018) and fanglomerate deposits (Tfg) from Ekren and others (1980) and Ekren and Byers, (1985; 1986a, b). Median density of unit is 2,226 kg/m<sup>3</sup> based on 3D gravity inversion modeling

## BEDROCK

### VOLCANIC ROCKS

- Tlf** **Mafic to intermediate lavas of Mount Ferguson (Miocene)**—Dominated by andesite lavas (Tlfa), lumped unit also consists of undivided volcanic rocks (Tlf), biotite rhyolite (Tlfb), breccia of intermediate-mafic lavas (Tlfbx), hypersthene andesite (Tlfp), flow-laminated quartz-latite (Tlfl), hornblende-pyroxene latite (Tlfh), hornblende quartz-latite (Tlfq), mafic intrusions (Tlmi), and mafic lavas (Tml) of Craig (2018), Ekren and others (1980), and Ekren and Byers (1985, 1986a, b). Median density of unit is 2,443 kg/m<sup>3</sup> based on 3D gravity inversion modeling
- Tp** **Poinsettia Tuff Member of Hu-pwi Rhyodacite (Miocene)**—Dominated by the Poinsettia Tuff Member of Hu-pwi Rhyodacite (Tp) and three associated distinct cooling units (Tpa, Tpb, Tpc) of Ekren and others (1980), and Ekren and Byers (1985, 1986a, b), this lumped unit also consists of undivided lavas (Tlp) and rhyolite lavas (Trl) of Craig (2018), Ekren and others (1980), and Ekren and Byers (1985, 1986a, b). Median density of unit is 2,464 kg/m<sup>3</sup> based on 3D gravity inversion modeling

### CRYSTALLINE BASEMENT ROCKS

- Tvc** **Metasedimentary and volcanoclastic rocks (Late Triassic)**—Thin bedded metamorphosed turbidites including laminated siltstone, claystone, and fine-grained sandstone and volcanoclastic rocks of the Luning Formation. Includes minor mafic to felsic intrusions, interbedded conglomerates, lava flows, and limestones (Craig, 2017; Ekren and others, 1980; and Ekren and Byers, 1985, 1986a, b). Median density of unit 2,717 kg/m<sup>3</sup> based on 3D gravity inversion modeling

## References Cited

- Angster, S.J., 2018, Contributions to the neotectonics of the central and northern Walker Lane: Reno, Nevada, University of Nevada, Ph.D dissertation, 172 p.
- Athens, N.D., Glen, J.M., Morin, R.L., and Klemperer, S.L., 2011, ATV magnetometer systems for efficient ground magnetic surveying: *The Leading Edge*, v. 30, p. 394–398.
- Ayling, B.F., 2020, 35 years of geothermal power generation in Nevada, USA—A review of field development, generation, and production histories: *Proceedings of the 45th Workshop on Geothermal Reservoir Engineering*, Stanford University, v. 45, 12 p.
- Bell, J.W., dePolo, C.M., Ramelli, A.R., Sarna-Wojcicki, A.M., and Meyer, C.E., 1999, Surface faulting and paleoseismic history of the 1932 Cedar Mountain earthquake area, west-central Nevada, and implications for modern tectonics of the Walker Lane: *Geological Society of America Bulletin*, v. 111, p. 791–807.
- Blakely, R.J., 1995, *Potential theory in gravity and magnetic applications*: Cambridge University Press, Cambridge, 464 p.
- Blakely, R.J., and Simpson, R.W., 1986, Approximating edges of source bodies from gravity or magnetic data: *Geophysics*, v. 51, p. 1494–1498, accessed May 20, 2020, at <https://doi.org/10.1190/1.1442197>.
- Bouligand, C., Glen, J.M., and Blakely, R.J., 2014, Distribution of buried hydrothermal alteration deduced from high-resolution magnetic surveys in Yellowstone National Park: *Journal of Geophysical Research—Solid Earth*, v. 119, no. 4, p. 2595–2630, accessed May 20, 2020, <https://doi.org/10.1002/2013JB010802>.
- Cockett, R., Kang, S., Heagy, L.J., Pidlisecky, A., and Oldenburg, D.W., 2015, SimPEG—An open source framework for simulation and gradient based parameter estimation in geophysical applications: *Computers and Geosciences*, v. 85, p. 142–154, accessed September 14, 2020, at <https://doi.org/10.1016/j.cageo.2015.09.015>.
- Colgan, J.P., Dumitru, T.A., Reiners, P.W., Wooden, J.L., Miller, E.L., 2006, Cenozoic tectonic evolution of the Basin and Range province in northwestern Nevada: *American Journal of Science*, v. 306, p. 616–654, accessed May 20, 2020, at <https://doi.org/10.2475/08.2006.02>.
- Coolbaugh, M.F., Raines, G.L., and Zehner, R.E., 2007, Assessment of exploration bias in data-driven predictive models and the estimation of undiscovered resources: *Natural Resources Research*, v. 16, no. 2, p. 199–207.
- Crafford, A.E.J., 2007, *Geologic map of Nevada*: U.S. Geological Survey Data Series 249, 1 CD-ROM, 46 p., 1 plate.
- Crafford, A.E.J., 2010, *Geological terrane map of Nevada*: Nevada Bureau of Mines and Geology Open-File Report 10–4, 1 plate, scale 1:500,000.

- Craig, J.W., 2018, Discovery and analysis of a blind geothermal system in southeastern Gabbs Valley, western Nevada: Reno, Nevada, University of Nevada, M.S. thesis, 110 p.
- Craig, J.W., Faulds, J.E., Hinz, N.H., Earney, T.E., Schermerhorn, W.D., Siler, D.L., Glen, J.M., Peacock, J., Coolbaugh, M.F., and Deoreo, S.B., 2021, Discovery and analysis of a blind geothermal system in southeastern Gabbs Valley, western Nevada, USA: *Geothermics*, v. 97, article 102177, accessed February 13, 2023 at <https://doi.org/10.1016/j.geothermics.2021.102177>.
- Craig, J.W., Faulds, J.E., Shevenell, L.A., and Hinz, N.H., 2017, Discovery and analysis of a potential blind geothermal system in southern Gabbs Valley, western Nevada: *Geothermal Resources Council Transactions*, v. 41, p. 2258–2264.
- Dynamic Graphics, Inc., 2018, *EarthVision Reference Manual*: Alameda, California, Dynamic Graphics, Inc, v. 10, 2,387 p.
- Earney, T.E., Schermerhorn, W.D., Glen, J.M., Peacock, J., Craig, J.W., Faulds, J.E., Hinz, N.H., and Siler, D.L., 2018, Geophysical investigations of a blind geothermal system in southern Gabbs Valley, Nevada: *Geothermal Resources Council Transactions*, v. 42, 14 p.
- Ekren, E.B., and Byers, F.M., Jr., 1985, Geologic map of the Gabbs Mountain, Mount Ferguson, Luning, and Sunrise Fault quadrangles, Mineral and Nye counties, Nevada: U.S. Geological Survey Miscellaneous Investigations Series Map I-1577, scale 1:48,000, 1 sheet.
- Ekren, E.B., and Byers, F.M., Jr., 1986a, Geologic map of the Mount Annie, Mount Annie NE, Ramsay Spring, and Mount Annie SE quadrangles, Mineral and Nye counties, Nevada: U.S. Geological Survey Miscellaneous Investigations Series Map I-1579, scale 1:48,000, 1 sheet.
- Ekren, E.B., and Byers, F.M., Jr., 1986b, Geologic map of the Murphys Well, Pilot Cone, Copper Mountain, and Poinsettia Spring quadrangles, Mineral County, Nevada: U.S. Geological Survey Miscellaneous Investigations Series Map I-1576, scale 1:48,000, 1 sheet.
- Ekren, E.B., Byers, F.M., Jr., Hardyman, R.F., Marvin, R.F., Silberman, M.L., 1980, Stratigraphy, preliminary petrology, and some structural features of Tertiary volcanic rocks in the Gabbs Valley and Gillis Ranges, Mineral County, Nevada: U.S. Geological Survey Bulletin 1464, 54 p.
- Faulds, J.E., Coolbaugh, M.F., Hinz, N.H., 2021, Inventory of structural settings for active geothermal systems and late Miocene (~8 Ma) to Quaternary epithermal mineral deposits in the Basin and Range province of Nevada: Nevada Bureau of Mines and Geology Report 58, 27 p., 3 plates, scale 1:2,500,000.
- Faulds, J.E., Coolbaugh, M.F., Vice, G.S., and Edwards, M.L., 2006, Characterizing structural controls of geothermal fields in the northwestern Great Basin—A progress report: *Geothermal Resources Council Transactions*, v. 30, p. 69–76.
- Faulds, J.E., Craig, J.W., Hinz, N.H., Coolbaugh, M.F., Glen, J.M.G., Earney, T.E., Schermerhorn, W.D., Peacock, J.R., Deoreo, S.B., and Siler, D.L., 2018, Discovery of a Blind Geothermal System in Southern Gabbs Valley, Western Nevada, through Application of the Play Fairway Analysis at Multiple Scales: *Geothermal Resources Council Transactions*, v. 42, 14 p.
- Faulds, J.E., Henry, C.D., and Hinz, N.H., 2005, Kinematics of the northern Walker Lane—An incipient transform fault along the Pacific-North American plate boundary: *Geology*, v. 33, p. 505–508, accessed May 7, 2020, at <https://doi.org/10.1130/G21274.1>.
- Faulds, J.E., Hinz, N.H., Coolbaugh, M.F., Cashman, P.H., Kratt, C., Dering, G.M., Edwards, J., Mayhew, B., and Mclachlan, H., 2011, Assessment of favorable structural settings of geothermal systems in the great basin, western USA: *Geothermal Resources Council Transactions*, v. 35, p. 777–784.
- Faulds, J.E., Hinz, N.H., Coolbaugh, M.F., Siler, D.L., Shevenell, L.A., Queen, J.H., DePolo, C.M., Hammond, W.C., and Kreemer, C., 2016b, Discovering geothermal systems in the Great Basin region—An integrated geologic, geochemical, and geophysical approach for establishing geothermal play fairways: Proceedings of the 41st Workshop on Geothermal Reservoir Engineering, Stanford University, v. 41, 15 p.
- Faulds, J.E., Hinz, N.H., Coolbaugh, M.F., Shevenell, L.A., and Siler, D.L., 2016a, The Nevada Play Fairway Project—Review of highly prospective areas for new discoveries of potentially viable geothermal systems in the Great Basin region, western USA: *Geothermal Resources Council Transactions*, v. 40, p. 535–540.
- Faulds, J.E., Hinz, N.H., Coolbaugh, M.F., Shevenell, L.A., Siler, D.L., Craig, M., Hammond, W.C., Kreemer, C., Oppliger, G., Wannamaker, P.E., Queen, J.H., and Visser, C.F., 2015b, Integrated geologic and geophysical approach for establishing geothermal play fairways and discovering blind geothermal systems in the Great Basin region, western USA—A Progress Report: *Geothermal Resources Council Transactions*, v. 39, p. 691–700.
- Hamm, S., Hass, E., Tasca, C., Winick, J., Augustine, C., Boyd, L., Dobson, P., Emmons, S., Gwinner, D., Hicks, A., Jelacic, A., Levine, A., Liu, X., McCabe, K., Mengers, J., Metcalfe, E., Millstein, D., Nieto, A., and Prisjatschew, A., 2019, *GeoVision—Harnessing the heat beneath our feet*: U.S. Department of Energy Geothermal Technologies Office Report, 218 p, accessed August 8, 2022 at <https://www.energy.gov/eere/geothermal/downloads/geovision-harnessing-heat-beneath-our-feet>.
- Ito, G., Frazer, N., Lautze, N., Thomas, D., Hinz, N., Waller, D., Whittier, R., and Wallin, E., 2017, Play fairway analysis of geothermal resources across the state of Hawaii—2. Resource probability mapping: *Geothermics*, v. 70, p. 393–405.
- Johnson, C.A., and Taylor, C.D., 2010, Three-dimensional modeling and visualization of Greens Creek drill-hole data, in Taylor, C.D., and Johnson, C.A., eds., *Geology, geochemistry, and genesis of the Greens Creek massive sulfide deposit, Admiralty Island, southeastern Alaska*: U.S. Geological Survey Professional Paper 1763, 429 p., 7 plates on CD.
- Kaven, J.O., Majer, E.L., Foxall, W., Sonnenthal, E.L., and Pettitt, W., 2019, Seismic hazard assessment at the Fallon, Nevada, Frontier Observatory for Research in Geothermal Energy site: U.S. Geological Survey Open-File Report 2019–1020, 16 p., accessed May, 15, 2020, <https://doi.org/10.3133/ofr20191020>.

- Kratt, C., Coolbaugh, M., Sladek, C., Zehner, R., Penfield, R., and Delwiche, B., 2008, A new gold pan for the west—Discovering blind geothermal systems with shallow temperature surveys: *Geothermal Resources Council Transactions*, v. 32, p. 153–158.
- Lautze, N., Thomas, D., Waller, D., Frazer, N., Hinz, N., and Apuzen-Ito, G., 2017, Play fairway analysis of geothermal resources across the state of Hawaii—3. Use of development viability criterion to prioritize future exploration targets: *Geothermics*, v. 70, p. 406–413.
- McClain, J.S., Dobson, P., Cantwell, C., Conrad, M., Ferguson, C., Fowler, A., Gasperikova, E., Glassley, W., Hawkes, S., Schiffman, P., Siler, D.L., Spycher, N., Ulrich, C., Zhang, Y., and Zierenberg, R., 2015, Geothermal play fairway analysis of potential geothermal resources in NE California, NW Nevada, and Southern Oregon—A transition between extension-hosted and volcanically-hosted geothermal fields: *Geothermal Resources Council Transactions*, v. 39, 4 p.
- Milicich, S.D., Pearson-Grant, S.C., Alcaraz, S., White, P.A. and Tschritter, C., 2018, 3D Geological modelling of the Taupo Volcanic Zone as a foundation for a geothermal reservoir model: *New Zealand Journal of Geology and Geophysics*, v. 61, no. 1, p. 79–95, accessed January 20, 2021, at <https://doi.org/10.1080/00288306.2017.1407346>.
- Moeck, I., Hinz, N.H., Faulds, J.E., Bell, J.W., Kell-Hills, A., and Louie, J., 2010, 3D geological mapping as a new method in geothermal exploration—A case study from central Nevada: *Geothermal Resources Council Transactions*, v. 34, p. 807–812.
- Muñoz, G., 2014, Exploring for Geothermal Resources with Electromagnetic Methods: *Surveys in Geophysics*, v. 35, p. 101–122, accessed May 7, 2020, at <https://doi.org/10.1007/s10712-013-9236-0>.
- Oldow, J.S., 1992, Late Cenozoic displacement partitioning in the northwest Great Basin, *in* Stewart, J.H., ed., *Geological Society of Nevada Walker Lane symposium: Structure, tectonics and mineralization of the Walker Lane*: Reno, Nevada, Geologic Society of Nevada, p. 17–52.
- Orenstein, R., and Delwiche, B., 2014, The Don A. Campbell Geothermal Project: *Geothermal Resources Council Transactions*, v. 38, p. 91–98.
- Peacock, J.R., Glen, J.M.G., Ritzinger, B., Earney, T.E., Schermerhorn, W.D., Siler D.L., and Anderson, M., 2018, Geophysical Imaging of Geothermal Systems Spanning Various Geologic Settings: *Geothermal Resources Council Transactions*, v. 42, 10 p.
- Phelps, G.A., Graymer, R.W., Jachens, R.C., Ponce, D.A., Simpson, R.W., and Wentworth, C.M., 2008, Three-dimensional geologic map of the Hayward fault zone, San Francisco Bay region, California: U.S. Geological Survey Scientific Investigations Map 3045, pamphlet 35 p., accessed January 11, 2021, at <https://pubs.usgs.gov/sim/3045/>.
- Ponce, D.A., 2021, Density and Magnetic Properties of Selected Rock Samples from the Western U.S. and Alaska: U.S. Geological Survey data release, <https://doi.org/10.5066/P9FONTGS>.
- Siler, D.L., 2022, Stratigraphic and fault surfaces from the Three-Dimensional Geologic Map of the southeastern Gabbs Valley Geothermal Area: U.S. Geological Survey data release, <https://doi.org/10.5066/P9BR3681>.
- Shervais, J.W., Glen, J.M., Liberty, L.M., Dobson, P., Gasperikova, E., Sonnenthal, E., Visser, C., Nielson, D., Garg, S., Evans, J.P., Siler, D.L., Deangelo, J., Athens, N., and Burns, E., 2015, Snake river plain play fairway analysis—Phase 1 report: *Geothermal Resources Council Transactions*, v. 39, 10 p.
- Shervais, J.W., Glen, J.M.G., Nielson, D.L., Garg, S., Liberty, L.M., Siler, D.L., Dobson, P., Gasperikova, E., Sonnenthal, E., Neupane, G., Deangelo, J., Newell, D.L., Evans, J.P., and Snyder, N., 2017, Geothermal Play Fairway Analysis of the Snake River plain—Phase 2: *Geothermal Resources Council Transactions*, v. 41, p. 2328–2345.
- Siler, D.L., and Faulds, J.E., 2013, Three-dimensional geothermal fairway mapping—Examples from the western Great Basin, USA: *Geothermal Resources Council Transactions*, v. 37, p. 327–332.
- Siler, D.L., Faulds, J.E., Glen, J.M.G., Hinz, N.H., Witter, J.B., Blake, K., Queen, J., and Fortuna, M., 2019a, Three-dimensional geologic map of the southern Carson Sink, Nevada, including the Fallon FORGE area: U.S. Geological Survey Scientific Investigations Map 3437, pamphlet 22 p., accessed November 7, 2020, at <https://doi.org/10.3133/sim3437>.
- Siler, D.L., Faulds, J.E., Hinz, N.H., Dering, G.M., Edwards, J.H., and Mayhew, B.M., 2019b, Three-dimensional geologic mapping to assess geothermal potential—Examples from Nevada and Oregon: *Geothermal Energy*, v. 7, no. 2, accessed October 1, 2019, at <https://doi.org/10.1186/s40517-018-0117-0>.
- Siler, D.L., Faulds, J.E., Mayhew, B., and McNamara, D.D., 2016a, Analysis of the favorability for geothermal fluid flow in 3D—Astor Pass geothermal prospect, Great Basin, northwestern Nevada, USA: *Geothermics*, v. 60, p. 1–12, accessed May 1, 2016, at <https://doi.org/10.1016/j.geothermics.2015.11.002>.
- Siler, D.L., Hinz, N.H., Faulds, J. E., and Queen, J., 2016b, 3D analysis of geothermal fluid flow favorability—Brady’s, Nevada, USA: *Proceedings of the 41st Workshop on Geothermal Reservoir Engineering*, Stanford University, 10 p.
- Siler, D.L., Zhang, Y., Spycher, N.F., Dobson, P.F., McClain, J.S., Gasperikova, E., Zierenberg, R.A., Schiffman, P., Ferguson, C., Fowler, A., and Cantwell, C., 2017, Play-fairway analysis for geothermal resources and exploration risk in the Modoc Plateau region: *Geothermics*, v. 69, p. 15–33, accessed May 7, 2020, at <https://doi.org/10.1016/j.geothermics.2017.04.003>.
- Telford, W.M., Geldart, L.P., and Sheriff, R.E., 1990, *Applied geophysics* (2d ed.): Cambridge, U.K., Cambridge University Press, 792 p.
- U.S. Geological Survey, 2020, Quaternary fault and fold database for the United States, accessed April 5, 2022, at <https://doi.org/10.5066/F7S75FJM>.

- Wernicke, B., 1992, Cenozoic extensional tectonics of the U.S. Cordillera, *in* Burchfiel, B.C., Lipman, P.W., Zoback, M.L., eds., *The Cordilleran Orogen; Conterminous U.S.—The Geology of North America*: Boulder, Colo., Geologic Society of America, p. 553–581.
- Wesnousky, S.G., 2005, Active faulting in the Walker Lane: *Tectonics*, v. 24, no. 3, 35 p., accessed May 7, 2020, at <https://doi.org/10.1029/2004TC001645>.
- Williams, C.F., Reed, M.J., DeAngelo, J., Galanis, S.P., Jr., 2009, Quantifying the undiscovered geothermal resources of the United States: *Geothermal Resources Council Transactions*, v. 33, 8 p.
- Williams, C.F., Reed, M.J., DeAngelo, J., and Galanis, S.P., Jr., 2007, The USGS national geothermal resource assessment—An update: *Geothermal Resources Council Transactions*, v. 31, p. 99–104.
- Williams, C.F., Reed, M.J., Mariner, R.H., DeAngelo, J., and Galanis, S.P., Jr., 2008, Assessment of Moderate- and High-Temperature Geothermal Resources of the United States: U.S. Geological Survey Fact Sheet 2008–3082, 4 p.
- Wilmarth, M., and Stimac, J., 2015, Power density in geothermal fields: *Proceedings of the World Geothermal Congress 2015*, 7 p.
- Witter, J.B., Siler, D.L., Faulds, J.E., and Hinz, N.H., 2016, 3D geophysical inversion modeling of gravity data to test the 3D geologic model of the Bradys geothermal area, Nevada, USA: *Geothermal Energy*, v. 4, no. 14, accessed January 9, 2020, at <https://doi.org/10.1186/s40517-016-0056-6>.
- Zha, X., Jia, Z., Dai, Z., and Lu, Z., 2019, The cause of the 2011 Hawthorne (Nevada) earthquake swarm constrained by seismic and InSAR methods: *Journal of Geodesy*, v. 93, p. 899–909, accessed June 1, 2020, at <https://doi.org/10.1007/s00190-018-1212-5>.
- Zheng, A., Chen, X., and Xu, W., 2020, Present-day deformation mechanism of the northeastern Mina deflection revealed by the 2020 Mw 6.5 Monte Cristo Range earthquake: *Geophysical Research Letters*, v. 47, no. 22, 10 p., accessed January 20, 2021, at <https://doi.org/10.1029/2020GL090142>.